Thesis Title

A DISSERTATION
SUBMITTED TO THE FACULTY OF THE GRADUATE SCHOOL
OF THE UNIVERSITY OF MINNESOTA
BY

Andy Jarod Julin

IN PARTIAL FULFILLMENT OF THE REQUIREMENTS
FOR THE DEGREE OF
DOCTOR OF PHILOSOPHY

Prof. Ron Poling

March, 2017

Acknowledgements

This is where the Acknowledgements go!

Dedication

This is where the Dedications go!

Abstract

We measure the production line shape of $e^+e^- \to \psi(3770) \to D\overline{D}$ around the nominal mass of the $\psi(3770)$. The $(70.05 \pm 0.03)\,\mathrm{pb}^{-1}$ of e^+e^- annihilation data used were collected in 2010 over an energy range of $3.735\,\mathrm{GeV}$ to $3.870\,\mathrm{GeV}$. Since the previously observed $e^+e^- \to D\overline{D}$ cross section cannot be explained by a single Breit-Wigner shape, this study investigates if interference effects from non-resonant $D\overline{D}$ production can account for the $D\overline{D}$ line shape.

Contents

List of Tables

List of Figures

Chapter 1

Introduction

Chapter 2

Theoretical Background

2.1 Standard Model

Developed throughout the 1960s and 1970s, the Standard Model provides the most complete description of observable matter in the universe to date. It is a classification of all confirmed subatomic particles currently known, and predicts the most accurate results of any scientific theory ever measured. Each of the electromagnetic, weak, and strong fundamental forces are well described by this formulation. These three are described by an $SU(3) \times SU(2) \times U(1)$ group, where the $SU(3)$ corresponds to the strong force, the $SU(2)$ corresponds to the weak force, and the $U(1)$ corresponds to the electromagnetic force. The remaining fundamental force, gravity, is negligible on the scale of the masses of fundamental particles, and will be ignored in the discussions that follow.

2.1.1 Electromagnetic Force

The electromagnetic force is responsible for attracting and repelling objects, most notably binding together electrons and protons to form atomic structures. The most prominent theory of electromagnetic interactions is known as Quantum Electrodynamics (QED). The mediator of this force is the photon, a massless vector boson. As there is only a single mediator, and a single conserved quantity (electric charge), the formulation of QED is relatively simple compared to the other forces. Still, the predictions it makes show astounding consistency with experiment, such as correctly calculating the anomalous magnetic dipole moment of the electron to more than 10 significant figures.

Much of this success is due to QED being expandable through perturbation theory, where corrections are applied in terms of higher order factors of the coupling constant, α. This is possible due to a relatively small coupling constant ($\alpha \approx 1/137$), as higher order terms are convergent.

2.1.2 Weak Force

The weak force is responsible for the decays of various particles into other forms. This is distinct from the electromagnetic and strong interactions, where the constituent particles cannot change their types (or flavors). The mediators of this force are the W and Z, which are massive vector bosons. Not only are each of these masses non-zero, they are considerably heavy particles at $80.4\,\text{GeV}$ and $90.2\,\text{GeV}$, respectively [1]. These large masses not only inhibit the interaction distance of the weak force, but also minimize the interaction strength (which is inversely proportion to mass). Furthermore, this mass excess also leads to much slower interaction times, further reducing the effects of the weak force in comparison to the strong and electromagnetic forces.

In addition to transforming particle flavor, the weak force is also unique in its violation of various symmetries. The first discovery of symmetry violation came in 1957, when Wu and others discovered the weak force did not behave identically under parity (P) transformations (i.e., mirror reflection). To account for this, a new theory conserving a compound symmetry was proposed. This combined charge conjugation (C), the swapping of particles with their antiparticles, with parity to form CP parity. However, in 1964, evidence of CP violation was also discovered by Cronin and Fitch. The resolution to this symmetry conservation involves yet a third symmetry, time reversal (T), in which time is replaced with its negative ($t \rightarrow -t$). While the weak force violates these symmetries individually, the application of all three (CPT) is conserved across all known processes.

At higher energy scales, the electromagnetic and weak forces unify into the electroweak force. In this theory, there are initially four massless gauge bosons mediating the interactions. Due to the Higgs mechanism, the initial gauge symmetry is broken at lower energies, and three of these bosons acquire a mass. These three bosons are the $W^{\pm}$ and Z, while the remaining massless boson is the γ. The energies scales required for this unification were only present in the early universe. Before this, it is also believed

there was an epoch of even higher energy, in which the electroweak force merged with the strong force.

2.1.3 Strong Force

The strong force is responsible for binding together particles known as hadrons. The most prominent theory of strong interactions is known as Quantum Chromodynamics (QCD). Like the electromagnetic force, the mediator of the strong force is also a massless vector boson, the gluon. However, while massless particles typically correspond to an infinite interaction range, the strong potential becomes very large at higher separations. This prevents particles which interact through the strong force from existing as isolated entities, and is known as confinement. The typical interaction range is on the order of the proton radius, around 10^{-15} m. QCD provides additional challenges, however, as the coupling constant is not small ($\alpha_S \gtrsim 1$). This excludes the use of perturbation theory for most cases, as the higher order terms do not converge.

Strong interactions are associated with a corresponding conserved quantity known as color charge. There are three colors associated with this charge, red (r), green (g), and blue (b). For anti-particles, there are oppositely charged values ($\bar{r}, \bar{g}$, and $\bar{b}$). In order for hadrons to be formed, the total color values of the constituents must be colorless. This means the total sum must involve all three colors (rgb or $\bar{r}\bar{g}\bar{b}$) or pairs of opposite colors ($r\bar{r}, g\bar{g}$, or $b\bar{b}$). However, these individual colors are not observable in nature. This effectively triples the number of possible particle combinations, due to combinatorics.

Unlike the photon, which is neutral to the electromagnetic force, the gluon also carries color charge. There are eight possible color combinations which a gluon may possess, which are typically expressed using the Gell-Mann representation of $SU(3)$. With this basis, each gluon is linearly independent, and no combination of gluons can be used to form a color singlet state. This inclusion of color by the force carrier makes QCD significantly more complex than QED. In fact, carrying color charge means gluons can also interact with each other directly, leading to certain theoretical states such as glueballs.

2.1.4   Elementary Particles

There are two primary groups contained in the Standard Model, fermions and boson. This division is based off the Spin Statistics theorem, where fermions have half-integer spins, and bosons have integer values. Because of these values, the Pauli Exclusion principle restricts fermions from occupying the same spatial state, and thus there are restrictions on their spatial density. Bosons, however, do not have this restriction, and can have any number occupying the same space. Thus, fermions are typically more tangible matter (such as electrons), while bosons typically represent the forces interacting between them (such as photons).

Fermions

The fermions are divided by their interaction types into two major groups, quarks (q) and leptons (l). Each of these groups contains six particles with their corresponding antiparticle. These can also be categorized into three generations, which aligns particles with the same electric charges, but greatly differing masses. For example, the up (u), charm (c), and top (t) quarks all have an electric charge of $+2/3$, but t is approximately five orders of magnitude more massive than u. In **??**, the rows indicate particles with the same electric charge, while the columns represent each generation of particles.

Although all fermions interact both electromagnetically and weakly, only the quarks interact strongly. Because of confinement, quarks cannot exist as isolated particles, and are only found in nature as groups of particles called hadrons. The most common types of hadrons exist as quark-antiquark pairs, known as mesons, or as groups of three quarks (or antiquarks), known as baryons. There are, however, indications of more exotic combinations of quarks, such as tetra- ($qq\bar{q}\bar{q}$) or penta-quark ($qqqq\bar{q}$) states seen by recent experiments.

While the negatively charged quarks (d, s, and b) are labeled as definite states, each of the quarks are actually mixed states. Through weak interactions, each of these quarks can transform into other states. The probabilities for these transformations are given by the Cabibbo-Kobayashi-Maskawa (CKM) Matrix, shown in Fig. **??**. Note that while the convention splits the negatively charged quarks into mixed states (leaving the positively charged quarks fixed), this choice has no physical basis. The reverse choice of having

mixed positively charged quarks is also valid.

The leptons are also divided into two major distinctions based on their charge. The electron (e^-), muon (μ^-), and tau (τ^-) are all negatively charged particles. With the exception of mass, the interaction properties of each flavor is very similar. However, the three flavors themselves are treated as separate conserved quantities. There is also a neutral particle, a neutrino (ν), corresponding to each one (ν_e, ν_μ, ν_τ). These are very small mass ($< 1\,\text{eV}$) particles with extremely low interactions.

The original formulation of the Standard Model assumed these neutrinos to be massless particles. However, this was violated by the discovery of neutrino oscillations, where transformations occur between neutrino flavor states due to differences in their masses. Additionally, the flavor states, ν_e, ν_μ, and ν_τ, are not the states observed in nature. Rather, the states with definite mass, labeled ν_1, ν_2, and ν_3, are linear combinations of the three flavor states. This can be expressed in a rotation of bases analogous to the CKM Matrix for quarks.

Bosons

For each of the three forces included in the Standard Model, there are accompanying gauge bosons. These include the photon (γ) for electromagnetic force, the W and Z for the weak force, and the gluon (g) for the strong force. Each of the gauge bosons are a spin-1 vector boson, which means there are three available polarization states (-1, 0, +1). However, since the photon and gluon are both massive, gauge invariance requires these to have transverse polarizations. This means the spin-0 state is eliminated, and there are only two polarization states for each. There is also the Higgs boson (H), which unifies the electromagnetic and weak forces, and whose interactions with other particles is responsible for their mass. This is the only known fundamental spin-0 particle, which means it has only one polarization state.

Even with the amazing success of the Standard Model, the theory is not complete. Along with neutrino oscillations, other effects, such as dark matter or dark energy, remain major hindrances in constructing a unified theory. Such a theory must also include gravity, but there remain significant difficulties in explaining its effects through a quantum field theory. There also remains no conclusive explanation for various constants, such as the masses of each fundamental particle. Still, the Standard Model remains the

most precise description of the universe to date, and continues to provide the basis for future experimental and theoretical work.

2.2   Charmonium

The majority of this analysis focuses on a specific group of particles known as Charmonium. These particles are resonances formed by a $c\bar{c}$ pair, and can be treated analogous to the hydrogen atom. Namely, there is a spectrum of various excited states in the Charmonium region, just as with the emission lines of hydrogen. The three states which are focused on include the $J/\psi, \psi'$, and ψ''. The ' and " marks indicate these are the first and second excited states of the J/ψ, respectively. More commonly, the ψ' is denoted $\psi(3686)$ and the ψ'' is denoted $\psi(3770)$. The numbers in parentheses represent the mass of the particle in MeV.

An alternative label for these states uses the quantum numbers for each particle. This is written in the form $N^{2s+1}L_J$, where N refers to the principal quantum number, s refers to the total spin of the particle, L refers to the angular momentum, and J refers to the total angular momentum. Here, the values of L are in spectroscopic notation, where $L = 1, 2, 3, 4 \ldots$ is denoted $S, P, D, F \ldots$, and higher values follow alphabetically (excluding J). As each of these states are comprised of two spin-$\frac{1}{2}$ particles, the value of s in this case can only be 0 (opposite) or 1 (aligned). With this, the $J/\psi, \psi(3686)$, and $\psi(3770)$ can be denoted 1^3S_1, 2^3S_1, and 1^3D_1. The values of n and L are used for the alternate notation of $\psi(2S)$ representing $\psi(3686)$. However, the notation of $\psi(1D)$ is not often used for $\psi(3770)$. This is due to evidence of mixing in $\psi(3770)$ between the 2^3S_1 and 1^3D_1 states that suggests more complicated underlying interactions [2, 3].

In fact, while the comparisons from this model work well for states less massive than the $\psi(3770)$, the predictions made above this often break down. This is likely based on the energy required to produce open-charm D mesons, such as $D^+(c\bar{u})$ and $D^0(c\bar{d})$. The $D\overline{D}$ threshold (twice the mass of the D^0) is just above the $\psi(2S)$ mass, and just slightly below the $\psi(3770)$ mass. Therefore, the decay products of the two particles end up being drastically different, even while the available phase space is relatively similar.

The difference is most clearly seen in the total decay widths, where the most recent

experimental averages [1] are $\Gamma^{\psi(2S)} = 286 \, \text{keV}$ and $\Gamma^{\psi(3770)} = 27.5 \, \text{MeV}$. An explanation for this discrepancy was proposed independently in the 1960s by Okubo [4], Zweig [5], and Iizuka [6], and is named the OZI rule. Effectively, any Feynman Diagram where the initial and final particles are separated at some point by only gluons represents a suppressed decay. This behavior requires that the momentum transfer from the initial particles must occur entirely through these gluons. Because of the decreasing strength of the strong interaction with higher momentum transfer, the rate of these decays is thereby inhibited. This is further compounded by the need for three gluons in such an interaction, as one gluon could not conserve color charge, and two could not converse C-parity. Once above the $D\overline{D}$ threshold, the allowed open-charm decays dominate, and the total width is massively increased. Such dominance points to a high branching fraction expected for decays of the type $\psi(3770) \to D\overline{D}$.

2.3 Derivation of $\sigma_{\psi(3770) \to D\overline{D}}$

The production rate for a pair of D mesons coming from $\psi(3770)$ at a given center-of-mass energy can be calculated following an approach of Kuraev and Fadin [7] applied by the KEDR collaboration [8]. This method also corrects for Initial State Radiation (ISR), affecting particles accelerated in a collider, and is given by the following:

$$\sigma_{D\overline{D}}^{RC}(W) = \int z_{D\overline{D}}(W\sqrt{1-x}) \, \sigma_{D\overline{D}}(W\sqrt{1-x}) \, \mathcal{F}(x, W^2) \, dx. \tag{2.1}$$

Here, W is the given center-of-mass energy, x is an approximation for the fraction of radiated energy, and $\mathcal{F}(x, W^2)$ is the probability of losing this energy from ISR:

$$\mathcal{F}(x, W^2) = \beta \, x^{\beta - 1} \left[1 + \frac{\alpha}{\pi} \left(\frac{\pi^2}{3} - \frac{1}{2} \right) + \frac{3}{4}\beta + \beta^2 \left(\frac{37}{96} - \frac{\pi^2}{12} - \frac{L}{72} \right) \right] = \beta \, x^{\beta - 1} F(W^2),$$
$$\beta = \frac{2\alpha}{\pi}(L - 1), \qquad L = \log \left(\frac{W^2}{m_e^2} \right). \tag{2.2}$$

The factor $z_{D\overline{D}}$ includes the expected Coulomb interaction between the mesons in of

the charged mode (D^+D^-),

$$z_{D^+D^-} = \frac{\pi\alpha/\beta_{D^+}}{1 - \exp(-\pi\alpha/\beta_{D^+})} \times \theta(W - 2m_{D^+}), \tag{2.3}$$

but only accounts for the $D\overline{D}$ energy threshold in the neutral mode $(D^0\overline{D^0})$,

$$z_{D^0\overline{D^0}} = \theta(W - 2m_{D^0}). \tag{2.4}$$

The theta function imposes the step in the cross section at the production threshold.

The integral in Eq. 2.1 can be simplified by taking advantage of the relatively constant values of $z_{D\overline{D}}$ and $\sigma_{D\overline{D}}$ over sufficiently small intervals. By splitting the full W range into such intervals and integrating over each, this becomes

$$\int \mathcal{F}(x, W^2) \, dx \approx \sum_{n=0}^{N} F(W^2) \int_{\frac{n}{N}}^{\frac{n+1}{N}} \beta x^{\beta-1} \, dx = \sum_{n}^{N} F(W^2) \left[x_{\text{upper}}^\beta - x_{\text{lower}}^\beta \right]. \tag{2.5}$$

The upper, lower, and mid-point values are given by

$$x_i = \left[1 - \left(\frac{2m_D}{W} \right)^2 \right] \left(\frac{n_i}{N} \right), \qquad n_i : \begin{cases} n_{\text{lower}} & = n \\ n_{\text{mid}} & = n + \frac{1}{2} \\ n_{\text{upper}} & = n + 1 \end{cases} . \tag{2.6}$$

The bracketed expression in Eq. 2.6 represents the maximum value of x determined by the theta functions of Eqs. 2.3 and 2.4. To maintain sufficient precision with this interval approximation, the value of $N = 1024$ is used. Combining this with the other factors in Eq. 2.1, the cross section including the effect of ISR becomes

$$\sigma_{D\overline{D}}^{RC}(W) = \sum_{n=0}^{N} z_{D\overline{D}}(W') \, \sigma_{D\overline{D}}(W') \, F(W^2) \left[1 - \left(\frac{2m_D}{W} \right)^2 \right]^\beta \left[\frac{[(n+1)^\beta - n^\beta]}{N^\beta} \right], \tag{2.7}$$

where $W' = W\sqrt{1 - x_{\text{mid}}}$. The Born level $D\overline{D}$ cross section is given theoretically by

$$\sigma_{D\overline{D}} = \frac{\pi\alpha^2}{3W^2} \beta_D^3 |F_D(W)|^2, \qquad \beta_D = \sqrt{1 - \frac{4m_D^2}{W^2}}. \tag{2.8}$$

Here, β_D is the velocity of the D meson in the center-of-mass system. The form factor F_D represents the contribution of each individual resonant (R) component and the total non-resonant (NR) component. Each resonant piece is parametrized with a phase angle relative to the non-resonant contribution:

$$F_D(W) = F_D^{\text{NR}}(W) + \sum_r F_D^{R_r}(W)\, e^{i\phi_r}. \tag{2.9}$$

Each resonant contribution to the form factor is modeled by a Breit-Wigner amplitude,

$$F_D^R(W) = \frac{6\, W \sqrt{(\Gamma_{ee}/\alpha^2)(\Gamma_{D\overline{D}}(W)/\beta_D^3)}}{M^2 - W^2 - iM\Gamma(W)}, \tag{2.10}$$

where Γ_{ee} is the electron partial width, and $\Gamma(W)$ represents the total width of the resonance with mass M:

$$\Gamma(W) = \left(\frac{M}{W}\right) \left[\frac{z_{D\overline{D}}(W)\, d_{D\overline{D}}(W)}{z_{D^0\overline{D^0}}(M)\, d_{D^0\overline{D^0}}(M) + z_{D^+D^-}(M)\, d_{D^+D^-}(M)}\right] \Gamma(M). \tag{2.11}$$

The value of $\Gamma(M)$ represents the total width at the nominal mass of the resonance. The factors $d_{D^+D^-}$ and $d_{D^0\overline{D^0}}$ are the Blatt-Weisskopf damping factors [9] for a vector resonance:

$$d_{D\overline{D}} = \frac{\rho_{D\overline{D}}^3}{\rho_{D\overline{D}}^2 + 1}, \qquad \rho_{D\overline{D}} = q_D R_0 = \left(\frac{\beta_D\, W}{2}\right) R_0. \tag{2.12}$$

Here, q_D is the D momentum in the center-of-mass frame, while R_0 represents the radius of the parent particle. The $D\overline{D}$ partial width listed in Eq. 2.10 is simply the total width rescaled according to $\mathcal{B}_{nD\overline{D}}$, the sum of all non-$D\overline{D}$ decay modes of $\psi(3770)$:

$$\Gamma_{D\overline{D}}(W) = \Gamma(W) \times (1 - \mathcal{B}_{nD\overline{D}}). \tag{2.13}$$

However, as a simplifying assumption, we use $\mathcal{B}_{nD\overline{D}} = 0$ throughout the analysis.

Chapter 3

Detector and Related Systems

All data used for this analysis were collected at the third Beijing Spectrometer (BESIII), located in Beijing, China, at the Institute of High Energy Physics (IHEP) campus. This detector records e^+e^- collision events provided by the second Beijing Electron-Positron Collider (BEPCII). The target energies for these collisions focus on τ^- and c production in the range of about $2.0\,\mathrm{GeV}$ to $4.6\,\mathrm{GeV}$. Both of these machines are upgrades from previous versions built on the same sites. The first BEPC and BES were originally constructed in 1989, while the upgrade to BESII occurred in 1996. These two sites were closed in 2004 to prepare for the upgrades to the current systems.

In 2009, BEPCII and BESIII resumed operation with the goal of utilizing greatly increased luminosity. For example, instead of the single-bunch electron collisions of BEPC, the new design utilized multiple bunch collisions. BEPCII also utilizes a dual-storage ring for the electrons and positrons, compared to the single-ring available at BEPC. The improvements provide BEPCII with a design luminosity of $10^{33}\,\mathrm{cm}^{-2}\,\mathrm{s}^{-1}$, two orders of magnitude larger than the previous installation. This luminosity is optimized for energies near the $\psi(3770)$ resonance, as BESIII conducts many precision measurements and rare decay searches around this region. A detailed description of the BESIII detector can be found in Ref. [10].

3.1 BEPCII Accelerator

The setup for collisions in BEPCII begins with bombarding a fixed target with electrons. This generates high energy photons which interact with the target material to form e^+e^- pairs. The positrons from these pairs are then separated magnetically. Using a linear accelerator, these positrons are then injected into the desired storage ring until they reach the desired beam current. As electrons do not need to be created in this manner, they are instead directly accelerated and injected into the opposite storage ring. These injections occur at a rate of $50\,\mathrm{mA/\,min}$ for positrons and $200\,\mathrm{mA/\,min}$ for electrons.

To achieve the necessary high beam currents, many bunches of electrons and positrons are packed into the evacuated rings. During operation, each ring contains 93 bunches spaced $8\,\mathrm{ns}$ ($2.4\,\mathrm{m}$) with a length of $1.5\,\mathrm{cm}$. These provide a beam current of $0.91\,\mathrm{A}$ while operating in collision mode. At the interaction point, each beam is focused using super-conducting quadrupole magnets to compress the beam size to about $5.7\,\mathrm{\mu m}$ vertically, while the horizontal beam size is about $380\,\mathrm{\mu m}$. For collisions, each beam is also angled towards the center of the storage rings with an angle of $11\,\mathrm{mrad}$. This crossing angle provides better resolution for determining particle momenta in the detector.

For a normal run, collisions continue occurring until the instantaneous luminosity falls below useful levels. While this is typically depleted due to the collisions between the e^+e^- particles, other unwanted interactions (such as those with beam-gas in the storage rings) also reduce these currents. When this happens, BEPCII can replenish the beams using top-off injections. This allows the collider to continue utilizing the remaining particles within the storage rings without dumping the beams completely. Recycling these leftover electrons and positrons saves considerable time, and allows for more efficient data taking.

3.2 BESIII Detector

Centered around the interaction point of BEPCII, the BESIII detector records information about the particles produced by the resulting collisions. Each collision occurs within the beam-pipe of the detector, which is used to minimize multiple-scatterings and secondary interactions. Its inner and outer radii are $31.5\,\mathrm{mm}$ and $57.0\,\mathrm{mm}$, and is pressurized to $5 \times 10^{-10}\,\mathrm{Torr}$. Surrounding the entire apparatus is a uniform, $1.0\,\mathrm{T}$

magnetic field provided by a super-conducting solenoid with a mean radius of $1.482\,\text{m}$ and a length of $3.53\,\text{m}$. The field points in the z-direction, which is along the direction of the e^+ beam. The x-direction points towards the center of the storage rings, while the y-direction is vertically upwards. This magnetic field is used to provide better precision on momenta measurements. An appropriate field strength curves the tracks of charged particles sufficiently to interact with more of the tracking volume, while minimizing those which curl too much to reach all layers of the detector.

The BESIII detector is split into four main layers which analyze different aspects for identifying particles. Starting from the most interior, these layers are the Multi-Layer Drift Chamber (MDC), the Time-of-Flight System (ToF), the Electromagnetic Calorimeter (EMC), and the Muon Identifier (MUC). Using the information provided by each layer, the particles seen in the detector are given a hypothesis for their most likely candidate. Only charged particles stable enough to sufficiently traverse the detector are identifiable in this way. The candidate particles identified at BESIII are electrons (e), muons (μ), pions (π), kaons (K), and protons (p). Short-lived particles, such as D^0 and D^+, must be reconstructed from their decays into these constituents, as well as neutral shower energy from photons (γ).

3.2.1 Multi-Layer Drift Chamber

The purpose of the Multi-Layer Drift Chamber is to determine the momenta and trajectories of charged particles. Because of the magnetic field encasing the detector, charged particles will travel in helical trajectories. The direction of travel is used to determine their charge, while the curvature of the track is used to determine their momenta.

The MDC is comprised of many layers of tungsten and sense wires to detect the ionization of particles which pass through its gas-filled volume. The tungsten wires create a constant electric field which causes ionized electrons to drift towards the sense wires. This field is tuned to a strength which minimizes secondary ionization. Conversely, the electric field near each of the sense wires is much larger than the rest of the volume. This forces an avalanche of secondary ionizations in order to create a current in the sense wires. The amount of energy deposited by this process is proportional to the original ionization levels. Tracing the path of energy depositions over time allows for the reconstruction of each charged particle trajectory.

The main design of the MDC focuses on a multi-layer assortment of cells corresponding to the individual sense wires. The inner and outer radii of the MDC are 59 mm and 810 mm, respectively. There are 43 layers of sense wires which cover 93% of the 4π solid angle in the detector. This provides position resolutions of 130 μm and 2 mm in the $r - \phi$ plane and beam direction, respectively, for each cell. The uncertainty in these measurements is dominated by electron diffusion and the readout time uncertainty for the electronics. For the transverse momentum, the resolution is about 0.5 % for tracks with momenta of 1 GeV, with uncertainties coming mainly from wire position measurements, and multiple scatterings from other material in the MDC.

The gas used for ionization is a mixture of 60% helium (He) and 40% methane (C_3H_8). Helium, being chemically inert, will not interact with the ionized electrons used to measure the position and deposited energy. Its low atomic number, and thus, long radiation length, also minimizes multiple scatterings which degrade the momentum resolution. Methane, with extra rotational and vibrational degrees of freedom not accessible to Helium, quenches the ionization energy. Without this effect, the ionization energy would not be diffused, and would degrade the measurements of deposited energy.

In addition to trajectory, the MDC also measures the rate of energy loss over distance for a particle traveling through a material [11],

$$-\frac{dE}{dx} = 4\pi N \frac{z^2 e^4}{m_e \beta^2} \left[\log \left(\frac{2m_e \beta^2}{I(1 - \beta^2)} \right) - \beta^2 \right], \tag{3.1}$$

where N is the electron number density of the material, z is the charge of the particle in terms of e, the charge of the electron, m_e is the mass of the electron, β is the velocity of the particle, and I is the mean excitation potential for electrons in the material being traversed. The resolution of dE/dx is about 6 % for particles incident 90° to the beam-axis. The uncertainty is due to fluctuations in the number of primary ionizations along the flight path, fluctuations in the avalanche process, as well as from edge effects on each cell.

The energy deposition provides a method of distinguishing particle candidates, as this quantity depends on the velocity of the particle. To identify a particle from the various candidates, the measured energy deposition (dE/dx_{meas}) is compared against the expected value (dE/dx_{exp}) of each hit used to reconstruct the particle's trajectory

(i):

$$\chi^2 = \sum_i \chi_i^2 = \left(\frac{dE/dx_{\text{meas}} - dE/dx_{\text{exp}}}{\sigma} \right)_i^2 , \tag{3.2}$$

where σ represents the uncertainty on the measured energy deposition. This process provides a separation of 3σ between K and π tracks with momenta up to $770\,\text{MeV}$.

3.2.2 Time-of-Flight System

The purpose of the Time-of-Flight System is to determine the velocity of charged particles. This is useful for distinguishing particles with similar momenta, but different masses. It uses information provided by the MDC to determine the probability for each charged track to match the possible particle hypotheses. Namely, this includes the measured momentum, the expected time interval based on its trajectory, and the mass for each particle hypothesis. This process provides a separation of 3σ between K and π tracks with momenta up to $900\,\text{MeV}$.

The ToF is comprised of two bands of staggered plastic scintillators attached to photomultiplier tubes (PMTs). These two bands, located at $0.81\,\text{m}$ and $0.86\,\text{m}$ from the beam-pipe, measure a time difference used to determine the speed of each charged particle. The resolution is about $100\,\text{ps}$, and is largely limited by the scintillation light rise time, as well as fluctuations associated with the PMTs. The layer is split into two regions, barrel and endcap, which cover the ranges $|\cos\theta| < 0.82$ and $0.85 < |\cos\theta| < 0.95$, respectively. The former is dual-layer with each containing 88 scintillators of $5\,\text{cm}$ thickness arranged in a trapezoidal cross section, while the latter contains two single layers of 48 fan-shaped scintillators. Between the two are support structures for the MDC as well as other service lines.

3.2.3 Electromagnetic Calorimeter

The purpose of the Electromagnetic Calorimeter is to determine the energy deposited by photons. Since each of the candidates identified in the detector will be relativistic, they are minimum ionizing particles. This causes each to deposit a relatively constant value of energy, independent of the measured momenta. However, electrons, with their extremely small mass, will deposit significant amounts of energy due to Bremsstrahlung radiation.

This provides a clear distinction in the detector between electron and muon tracks above 200 MeV. Energy measurements from the EMC are also useful for identifying neutral particles which decay only to photons, such as π^0.

The EMC is comprised of tellurium-doped cesium iodide (CsI(Tl)) crystals with square front faces attached to a photodiode. Each of the 6240 crystals are 5.2 cm long on the square edges and 28 cm (15 radiation lengths) deep. To prevent photons from aligning with the gaps between each crystal, each one is offset with a tilt of $1.5°$ in the ϕ-direction and $1.5°$ to $3°$ in the θ-direction. These crystals provide an energy resolution (σ/E) of 2.5% at 1 GeV and 4% down to 100 MeV. This is limited by energy not deposited over the length of the crystal, the areas between crystals, and by non-uniform light production. Additionally, only measurements of energy above 20 MeV are considered, as below this value is indistinguishable from noise. The position resolution is $\sigma = 0.6\,\mathrm{cm}/\sqrt{E\ [\mathrm{GeV}]}$, and is primarily limited by the crystal segmentation. The layer has an inner radius of 94 cm and a total weight of approximately 24 tons. It covers the regions $|\cos\theta| < 0.83$ (barrel) and $0.85 < |\cos\theta| < 0.93$ (endcap), but does not well capture the region between the two.

3.2.4 Muon Identifier

The purpose of the Muon Identifier is to determine the likelihood of a charged particle being a muon. Since electrons are significantly lower mass, they deposit virtually all of their remaining energy in the EMC. Additionally, since muons do not interact strongly, they will penetrate notably further than will pions, kaons, or protons. This provides a clear indication of a muon when a particle traverses much of the MUC layer. However, due to the magnetic field, only muons with $p > 0.4$ GeV will be able to traverse deep enough to be identifiable.

The MUC is comprised of resistive plate counters (RPC) which are interspersed between the steel plates of the super-conducting solenoid. Each of the steel layers generally increase in thickness working outwards from the center: 3 cm, 3 cm, 3 cm, 4 cm, 4 cm, 8 cm, 8 cm, 8 cm, and 15 cm. Like the other layers, the MUC is also split into a barrel and an endcap region. The barrel has nine RPC layers of 4 cm thickness. In the endcap, the first RPC layer is after the first steel layer, leaving only eight RPC layers. Each of these layers have RPC strips oriented along only one direction. For the

barrel, the z (ϕ) orientation is read out for only the odd (even) layers. Conversely, the endcap only reads out the x (y) orientation in the odd (even) layers.

3.3 Triggering Systems

In order to maintain a high efficiency for selecting physics events, many backgrounds must be filtered out. At BESIII, this is done through a triggering system with two-tiers: a hardware trigger (L1) and a software event filter (L3). This process is illustrated in Fig. **??**. The filtered background events are primarily from beam-related sources, such as beam-gas or beam-wall interactions, and occur at a rate of about 13 MHz. To assist with this process, collimators and masks are used to prevent lost electrons from interacting with the detector. However, there are also other sources of backgrounds, such as cosmic rays, which occur at a rate of about 1.5 kHz. The total backgrounds must be suppressed to a rate which does not overwhelm the recording of events by the readout systems. This rate is roughly 2 kHz at the J/ψ peak, and 600 Hz for the $\psi(2S)$ when running near peak luminosity. For Bhabha events ($e^+e^- \to e^+e^-$), which are used for calibration and luminosity measurements, this rate is 800 Hz within detector acceptance.

The first step (L1) reads out every clock cycle (24 ns) at a rate of 41.65 MHz. It uses information from the MDC, ToF, and EMC collectively to reduce the rates of beam-related backgrounds to 1.84 kHz and cosmic rays to about 200 Hz. However, L1 has a maximum rate of about 4 kHz. Because of this, when the buffer holding the subdetector data is around 80 % full, L1 triggering is halted until the buffer drops below 10 % full. The efficiency of the L1 process is summarized in Table **??**.

From the MDC, L1 gathers information about each charged track. The main parameter examined is the number of superlayers a track passed through. These are defined as 'short' tracks if they deposit energy in segments of superlayers 3-5, or 'long' tracks for superlayers 3-5 and 10. To ensure a sufficient momentum to reach the outer superlayers while originating at the interaction point, a minimum transverse momentum cut is applied to each track. This cut is 90 MeV and 120 MeV for short and long tracks, respectively. In addition to the numbers of short and long tracks for an event, the information about back-to-back tracks is also used.

From the ToF, L1 gathers information about the number of hits in the barrel and end-cap regions. It also examines the number of back-to-back hits in each of the two regions. Here, 'back-to-back' is defined as having hits within a range of 9 counters on the opposite side of the detector.

From the EMC, L1 gathers information about the clustering of energies around a local maximum-energy crystal. This includes the number of isolated clusters, as well as the information about back-to-back hits in the barrel and end-cap. Additionally, the balance of energy in the ϕ-direction (barrel) and in the z-direction (endcap) is also used.

The subdetector information gathered during L1 is then passed off to an online computer farm (L3) where the event is assembled. This step reduces backgrounds from a rate of about $2\,\mathrm{kHz}$ to about $1\,\mathrm{kHz}$. Combined with the signal rate at the J/ψ peak $(2\,\mathrm{kHz})$, this corresponds to a total event rate of $3\,\mathrm{kHz}$, or a tape write speed of $40\,\mathrm{MB/s}$.

Chapter 4

Analysis Software

4.1 BESIII Offline Software System

Reconstructing and processing event data gathered by the BESIII detector is done using the BESIII Offline Software System (BOSS) [12]. This is an analysis software distribution written using the C++ language and running primarily on the Scientific Linux CERN operating system [13]. There are five main parts to BOSS: framework, simulation, reconstruction, calibration, and analysis.

4.1.1 Framework

The framework is built on the Gaudi software architecture [14], which provides a standard interface and utilities for things such as event simulation, data processing, and physics analysis. The software is managed using the Configuration Management Tool [15], which provides a method for creating packages, handling package dependencies, and producing executables from source code. There are three main filetypes for data stored by the framework: raw data (`.raw`), reconstructed data (`.rec`), and Data-Summary-Tape (`.dst`). The latter two of these file types are derived from the ROOT [16] format (`.root`) for easy management and usage in various analyses.

4.1.2 Simulation

There are four main parts to the simulation process: event generation, detector description, particle tracking, and detector response. Event generation is primarily handled by the Monte Carlo (MC) generators KKMC, BesEvtGen, and Babayaga, which are described below. To model its geometry and materials, a unique description of the detector has been created using a format based on XML. This allows both simulation and reconstruction packages to appropriately model the behavior of events within the specific environment of BESIII. For particle tracking, interactions with detector materials are handled by GEANT4 [17]. Lastly, detector responses are modeled by the so-called 'digitization code'. This takes into account each detector component, as well as readout electronics, and realistic situation such as noise or dead channels. There is also a simulation of the trigger systems implemented.

KKMC

Originally developed for the LEP and SLC colliders, KKMC [18] is a generator used to model electroweak interactions. Namely, the processes generated are of the form $e^+e^- \to f\bar{f} + (n)\gamma$, where $f = \{\mu, \tau, u, d, s, c, b\}$, and $(n)\gamma$ represents any number of additional photons. These are modeled taking into account second-order sub-leading corrections, as well as initial-state radiation, and interference between initial- and final-state radiation. The effects of beam energy spread, typically on the order of $1\,\mathrm{MeV}$ near the $\psi(3770)$, can also be included.

   After generation, the $f\bar{f}$ pair is decayed by models depending on the fermions involved. The TAUOLA library [19] is used to decay $\tau^-\tau^+$ pairs, and takes into account spin-polarization effects. The PYTHIA model [20] is used to hadronize final-state $q\bar{q}$ continuum production using the parton shower model. For resonances like the $\psi(3770)$, the only action performed by KKMC is the generation of ISR. After this, the virtual photon produced is handed off to BesEvtGen.

BesEvtGen

Originally developed for the CLEO and BaBar collaborations, EvtGen [21] is another widely used generator. It is the basis for BesEvtGen [22], which incorporates many

different decay models into a single utility. Over 30 exclusive decay models are available in BesEvtGen, as well as the capability to incorporate user-created models.

The decay process occurs sequentially using dynamic information from amplitude probabilities and forward / backward spin-density matrices. From this, final state radiation is handled by the PHOTOS model [23]. To generate unknown decays of charmonium resonances, the LundCharm model [24] is used, while other unknown hadronic decays are handled by PYTHIA. For radiative processes, such as radiative return to J/ψ or $\psi(2S)$, the VECTORISR model [25] is used. This occurs when one particle in the initial e^+e^- pair radiates a photon of high enough energy that only lower mass resonances can be produced from the reduced center-of-mass energy. When the radiation is less intense, the $\psi(3770)$ resonance is directly produced through the combination of KKMC and BesEvtGen.

Babayaga

Production of QED processes is done using the Babayaga generator [26]. This includes $e^+e^- \rightarrow \{e^+e^-, \mu^+\mu^-, \gamma\gamma\}$. The results are of very high precision, with an estimated theoretical accuracy of 0.1 %. It also matches exact next-leading-order corrections from the parton shower algorithm. The high precision also helps determine the efficiencies and acceptances required to precisely measure the integrated luminosities of each data sample.

4.1.3   Reconstruction

Reconstruction primarily involves information about specific types of particles from each of the four main detector layers. These sources of information are as follows:

- a charged track finding algorithm and a Kalman-filter-based track-fitter

- a particle identifying algorithm based on dE/dx and time-of-flight measurements

- a shower- and cluster-finding algorithm for EMC energy and position

- a muon track finding algorithm

Further descriptions about each of these processes can be found in Sec. 4.2. Additionally, algorithms for determining the corresponding beam bunch crossing, as well as for secondary vertex and track refitting, are also utilized.

4.1.4 Calibration

To maintain consistent production and analysis of datasets, a centralized source of run-dependent information is maintained by BOSS. This includes algorithms which determine the calibration constants for each sub-detector, as well as a centralized database to store the results. Each of the calibration outputs are stored in a ROOT file along with other details such as the beam energy, luminosity, magnetic field information, trigger conditions, and hardware / software versions. While all of this information is stored by a central MySQL [27] server at IHEP, databases for other institutions in BESIII regularly synchronize with this server to create a mirrored copy of these values.

4.1.5 Analysis

4.2 Detector Simulation

The following sections detail the simulation, calibration, and reconstruction processes for each layer. Each of these relies on a geometry description created using GEANT4.

4.2.1 Multi-Layer Drift Chamber

Simulating events in the MDC accounts for the axial layers and endplates, the stereo layers, and the stereo cells. The simulation also heavily relies on the calibration parameters to determine things such as wire efficiency and resolution as a function of drift distance for each wire, noise in each layer, and other misalignment issues.

Calibration of the MDC uses $J/\psi \to \mu^+\mu^-$ events to determine position and dE/dx measurements. Using J/ψ events allows for quickly obtaining sufficient statistics due to the very large production cross section at the peak. The information determined includes constants such as $x - t$ relations, timing, alignment, and absolute wire efficiency. Each of these values are stored in the database for each run. Additionally, turning off the magnetic field could allow for precise determination of wire positions.

Reconstructing MDC events starts by finding axial track segments using raw hits. Each of these are found by searching for pre-calculated patterns. Next, these segments are linked to circular tracks by a circular fit using the least-squares method. Stereo segments are then added using an iterative helix fit. Lastly, additional hits which were possibly missed from the initial reconstruction are applied using a Kalman-filter process. This process also examines the tracks over multiple particle hypotheses. The reconstruction is remarkably efficient, with over $98\,\%$ of tracks with $p_T > 150\,\text{MeV}$ being reconstructed, even amidst high backgrounds. From this, the charge, momentum, and trajectory can be determined for each track.

In addition to tracking, the MDC also analyzes dE/dx for each particle. This calculates the energy deposition of each track as it passes through the chamber, and corrects the measured charge amplitudes to determine a probability for each particle hypothesis. Corrections applied account for things such as multiple scatterings, magnetic deflections, and ionization. This likelihood from dE/dx is used in conjunction with information from the ToF to identify the actual type of particle for each track.

4.2.2   Time-of-Flight System

Simulating events in the ToF accounts for the scintillator, wrapping materials, and photomultiplier tubes. The process converts the energy deposited in the scintillator into photons, then propagates the shape of a photon pulse (rather than individual photons) to the PMTs in order to generate an electronic signal. A discriminator is applied to each pulse to determine the analog-to-digital conversion (ADC) and time-to-digital conversion (TDC) outputs. The algorithm is tested using the results of beam tests, however, subsequently gathered data sets require updated tuning. A full simulation tracing each optical photon can also be used for further details on the timing measurement.

Calibration of the ToF also uses J/ψ decays to leptons to determine both timing and energy measurements. The information determined includes effective velocity, attenuation length, and muon energy loss. The status and performance of the ToF are also regularly monitored by a laser-fiberoptics pulsing system.

Reconstructing ToF events starts by using tracks with trajectories extrapolated from the MDC. Each track is then matched with a particular ToF module; either the two layers of the barrel, or the single-layer endcap. The travel time for each hypothesis

is then calculated using a weighted average of results from PMTs at both ends of the scintillator. Corrections are also applied to account for aspects like the effective light velocity in the scintillator and the light attenuation length. Measurements of dE/dx are obtained for both charged and neutral particles, and are added back into the EMC in order to improve the shower energy resolution.

4.2.3 Electromagnetic Calorimeter

Simulating events in the EMC accounts for the crystals, casing, silicon photodiodes, preamplifier boxes, cables, and the support system. For each of the crystals and photodiodes, hit information is recorded, and the deposited energy is summed. From this, photon statistics are computed, and the resulting photodiode response is converted into electronic signals. To obtain the waveform in the time domain, an inverse Laplace transform is applied. Then, a sampling and peak searching process is simulated to yield energy and time information. For each bin, Gaussian-type electronic noise is added, and the background is produced by summing over the waveforms.

Calibration of the EMC uses Bhabha electrons with $E > 1.55\,\text{GeV}$ for the high energy response, and $\pi^0 \to \gamma\gamma$ decays for the low energy response. The responses for individual crystals must be analyzed separately, due to their potential intrinsic variations. As a result, they are monitored frequently by a LED light pulser, and periodically recalibrated. Corrections due to temperature variations can also be applied.

Reconstructing EMC events starts by converting the ADC value of each crystal into energy based on the calibration constants. After this, clusters in both the barrel and endcaps are formed by analyzing local maximum energy deposits, called seeds. A clustering algorithm then relates hits around these seeds and sums the values for a particular shower. The positions of each shower is then calculated using energy-weighted first moments. If multiple seeds are found in one cluster, a splitting algorithm is invoked to split the cluster into multiple showers. Additionally, matching energy deposits from the ToF are also added back into the total shower energy. This improves the energy resolution, particularly for low energy photons.

4.2.4 Muon Identifier

Simulating events in the MUC accounts for forming each RPC, creating sets of strips to form each read-out plane, combining each of these with aluminum boxes to form a muon counter module, and placing the modules alongside iron slabs. The digitization from the read-out planes is selected to fire based off the distance away of each track. Noise is simulated using Poisson distributions initially determined from measurements made during the construction of the chamber, and updated with the taking of actual data.

Calibration of the MUC analyzes RPC detection efficiencies over a function of area. The cluster size and noise levels are also studied.

Reconstructing MUC events starts by searching for collected hits in each of the barrel and endcap orientations. The two collections are then combined with reconstructed tracks from the MDC. Since low momentum muons may cause only a few layers to fire, a subsequent search is performed over unused hits based on the extrapolated trajectories of MDC tracks. The reconstruction process primarily analyzes the depth of the track in the MUC, the maximum number of hits in the layers fired by a track, and the matching between a MDC track with the MUC stand-alone track. These parameters, along with the track momentum and MDC exit angle, are input into an Artificial Neural Network in order to distinguish between hadron and muon tracks. The distinction process is quite effective, generally removing $\sim 96\,\%$ of pions and keeping around $\sim 90\,\%$ of muons.

4.3 D-Tagging

From the decay of the $\psi(3770)$, the most commonly produced particles are $D^0\overline{D^0}$ or D^+D^- pairs. Since the $D\overline{D}$ pairs produced are two-body decays, the energy available to each D is half of the center-of-mass energy (in the center-of-mass reference frame). Each of these D mesons then quickly decays to certain sets of particles. Reconstructing one of these decays requires assembling the right combination of such particles. From energy and momentum conservation, the total 4-momentum of the constituents must match the total energy of the D meson.

This reconstruction technique is known as 'D-Tagging', and was pioneered by the MARK-III collaboration [28, 29]. For our analysis, the particles analyzed in the detector

include $\pi^{\pm}, K^{\pm}, \pi^0$, and K_S^0, and the decay modes used are shown in Table 4.1. There are three D^0 modes and six D^+ modes, where charge conjugation (converting all particles to their anti-particles) is implied throughout the analysis. The modes used are chosen for their effectiveness of reconstruction in the detector; they generally have higher branching fractions and minimize multiplicity (the number of tracks used). Additionally, for the neutral modes, the doubly-Cabbibo suppressed decays (DCSD), such as $D^0 \to K^+ \pi^-$, are also included by this procedure.

(0) $D^0 \to K^- \pi^+$	(200) $D^+ \to K^- \pi^+ \pi^+$	(203) $D^+ \to K_S^0 \pi^+ \pi^0$
(1) $D^0 \to K^- \pi^+ \pi^0$	(201) $D^+ \to K^- \pi^+ \pi^+ \pi^0$	(204) $D^+ \to K_S^0 \pi^+ \pi^+ \pi^-$
(3) $D^0 \to K^- \pi^+ \pi^+ \pi^-$	(202) $D^+ \to K_S^0 \pi^+$	(205) $D^+ \to K^+ K^- \pi^+$

Table 4.1: The reconstructed D-tag modes used in this analysis.

This process occurs for each event and searches over each decay mode for each charm (i.e., both D^+ and D^-). The combinations chosen for reconstruction are those with the smallest energy difference from the expected value. More than one D combination can be extracted from a given event, as long as it satisfies all other requirements (see Section 4.3.1). While this may sound like it overestimates the number of actual D particles found, the process is also used to calculate reconstruction efficiency, and will cancel out this effect.

4.3.1 Selection Cuts

Before being considered as potential reconstruction candidates, each track in the detector must also pass other cuts specific to its identified particle type. The following describes the necessary criteria required for the particles in the decay modes we are using.

$\pi^{\pm}/K^{\pm}$ Selection

Each of the reconstructed charged tracks must pass vertex cuts in both the transverse $(x - y)$ and beam (z) directions relative to the interaction point. This requires tracks originate sufficiently close to the interaction point to ensure they are not other backgrounds, such as cosmic rays, or other tracks which have decayed in flight. There is also a cut on the angle measured within the MDC (θ) to ensure the track has not disappeared

down the beam-line (where detection cannot occur). Lastly, from the particle identification process, the probability of being a pion (kaon) must be more likely than being a kaon (pion). The values for each of these requirements can be found in Table 4.2.

Vertex (xy)	$V_{xy} < \ 1\,\mathrm{cm}$
Vertex (z)	$|Vz| < 10\,\mathrm{cm}$
MDC Angle	$|\cos\theta| < 0.93$
Pion Probability	$P(\pi) > 0, \quad P(\pi) > P(K)$
Kaon Probability	$P(K) > 0, \quad P(K) > P(\pi)$

Table 4.2: The required cuts to identify charged tracks as $\pi^{\pm}$ or $K^{\pm}$.

γ Selection

To distinguish photon energy from noise, each shower in the EMC is required to have a certain amount of deposited energy. These cuts are different for the barrel ($|\cos\theta| <$ 0.80) and endcap ($0.84 < |\cos\theta| < 0.92$) regions. Each photon must also pass a TDC timing cut to ensure they are consistent with actual physics events, and not originating at other times. The values for each of these requirements can be found in Table 4.3.

Minimum Energy (Barrel)	$25\,\mathrm{MeV}$
Minimum Energy (Endcap)	$50\,\mathrm{MeV}$
TDC Timing	$t < 14 \times 50\,\mathrm{ns}$

Table 4.3: The required cuts to identify neutral showers as a γ.

π^0 Selection

Reconstructing π^0 mesons involves finding $\gamma\gamma$ pairs, as this is its most dominant decay ($\sim$99 %). Each of the γ showers used must pass the cuts described above. Additionally, at least one photon in the pair must be found in the barrel region. Each of the two photons are then kinematically fit to compare with the invariant mass of the π^0, and must also pass a proper fit cut. The resulting momentum from this fit is used for reconstructing D-tag candidates. The values used for each of these requirements are shown in Table 4.4.

Nominal Mass	$115\,\text{MeV} < m_{\pi^0} < 150\,\text{MeV}$
Fit Quality	$\chi^2 < 200$, Converged

Table 4.4: The required cuts to reconstruct $\gamma\gamma$ pairs as a π^0.

K_S^0 Selection

Reconstructing K_S^0 mesons involves finding $\pi^+\pi^-$ pairs, as this is its most common decay ($\sim$70 %). While $\pi^0\pi^0$ pairs are also a substantial decay mode ($\sim$30 %), these are not considered for reconstruction due to the increased difficulty of finding correct 4γ sets. To account for the K_S^0 decaying in flight, each of the charged pions considered are not subjected to the vertex or probability cuts in Table 4.2. Instead, the two found pions are kinematically constrained to a common vertex. The results must pass a nominal mass cut ($\sim$3 σ) and a proper fit cut to be deemed a K_S^0. From this, the resulting momentum from the vertex fit is used for reconstructing D-tag candidates. The values used for each of these requirements are shown in Table 4.5.

Nominal Mass	$487\,\text{MeV} < m_{K_S^0} < 511\,\text{MeV}$
Fit Quality	$\chi^2 < 100$, Converged

Table 4.5: The required cuts to reconstruct $\pi^+\pi^-$ pairs as a K_S^0.

Cosmic Ray and Lepton Veto

Lastly, when reconstructing the mode $D^0 \to K^-\pi^+$, an additional veto is used. Since the mode has only two charged tracks, it is common to misidentify particles which come from cosmic ray and two-lepton backgrounds. To prevent this, cuts on the timing difference between the tracks, as well as on the particle identification process, are enacted. The values used for each of these requirements are shown in Table 4.6.

Timing (TDC)	$|t_1 - t_2| < 5 \times 50\,\text{ns}$
Particle Identification	$(\chi^2_{e^-} + \chi^2_{e^+}) - (\chi^2_{K^-} + \chi^2_{\pi^+}) > 10$

Table 4.6: Cuts to prevent cosmic ray and lepton backgrounds in $D^0 \to K^-\pi^+$.

4.3.2 Reconstruction

After each of the constituent particles are identified, a reconstructed D candidate can be characterized by two main properties:

$$\Delta E = |E_{\text{beam}} - E_{\text{tag}}|, \qquad m_{\text{BC}} = \sqrt{E_{\text{beam}}^2 - |\vec{p_{\text{tag}}}|^2}. \qquad (4.1)$$

These are the energy difference (ΔE) and the beam-constrained mass (m_{BC}), and effectively represent the energy and momentum of the D-tag, respectively. As the candidate with the smallest ΔE for each decay mode in each event is selected, the values will typically peak near $0\,\text{MeV}$. Distributions of m_{BC}, meanwhile, typically peak near $m_{D^0} = 1.865\,\text{GeV}$ or $m_{D^+} = 1.870\,\text{GeV}$. Additionally, while invariant mass ($m_{\text{inv}} = \sqrt{E_{\text{tag}}^2 - |\vec{p_{\text{tag}}}|^2}$) can also be examined, m_{BC} is generally preferred due to a higher precision for the beam energy than of the individual particles comprising the D candidate.

Chapter 5

Measurement of $\sigma_{D\overline{D}}$ near $\psi(3770)$

5.1 Form Factors

In Eq. 2.9, we assume the $\psi(2S)$ resonant contribution is negligible in the energy range of our measurements, so the only major resonant contribution is from the $\psi(3770)$:

$$F_D(W) = F_D^{\text{NR}}(W) + F_D^{\psi(3770)}(W)\, e^{i\phi^{\psi(3770)}}. \tag{5.1}$$

Currently, there is no definitive model for the non-resonant term, so we use two alternative parameterizations for this. The first is a simple exponential model:

$$F_D^{NR} = F_{NR}\, \exp(-q_D^2/a_{NR}^2), \tag{5.2}$$

where both F_{NR} and a_{NR} are parameters determined through fitting. The second treatment implements a Vector Dominance Model (VDM). This assumes the interference effects are due to the $\psi(2S)$ mediating $D\overline{D}$ production above threshold,

$$F_D^{NR}(W) = F_D^{\psi(2S)}(W) + F_0, \tag{5.3}$$

and that the effective properties of the $\psi(2S)$ are similar to those of the $\psi(3770)$. The real constant F_0 represents the potential effect of higher resonances, like the $\psi(4040)$.

The first term is similar to Eq. 2.10, but with a modification to the total width:

$$\Gamma^{\psi(2S)}(W) = \left(\frac{M^{\psi(2S)}}{W}\right)\left[\frac{z_{D^0\overline{D^0}}(W)\,d_{D^0\overline{D^0}}(W) + z_{D^+D^-}(W)\,d_{D^+D^-}(W)}{z_{D^0\overline{D^0}}(M^{\psi''})\,d_{D^0\overline{D^0}}(M^{\psi''}) + z_{D^+D^-}(M^{\psi''})\,d_{D^+D^-}(M^{\psi''})}\right]\Gamma^{\psi(2S)}(M).$$
$$(5.4)$$

Without this modification, the mass of the $\psi(2S)$ would be below the $D\overline{D}$ threshold, and thus, the vanishing $z_{D\overline{D}}$ terms would cause a singularity in the width. Therefore, we use the mass of the $\psi(3770)$ in its place to estimate the effects in this region. While it may behave like the total width in Eq. 5.4, the true the physical meaning of the parameter $\Gamma^{\psi(2S)}(W)$ is uncertain. For the radii in Eq. 2.12, however, the values used are distinct for each meson: $R_{\psi(2S)} = 0.75\,\mathrm{fm}$ and $R_{\psi(3770)} = 1.00\,\mathrm{fm}$.

5.2   Data and Monte Carlo Samples

5.2.1   Data Samples

This analysis primarily uses scan data produced by BEPCII and collected by BESIII in 2010 over an energy range of $3.643\,\mathrm{GeV}$ to $3.890\,\mathrm{GeV}$. These data are partitioned into 35 center-of-mass energy (E_{cm}) bins of variable size over a range of $3.735\,\mathrm{GeV}$ to $3.870\,\mathrm{GeV}$. The range was chosen to be above the $D^0\overline{D^0}$ threshold $(3.730\,\mathrm{GeV})$ and below the $D^{*0}\overline{D^0}$ threshold $(3.872\,\mathrm{GeV})$. This range includes bins which are below the threshold for D^+D^- $(3.739\,\mathrm{GeV})$, with production beginning in the fourth bin.

Additionally, there are three higher statistics points used for comparison. These include an 'On-Peak $\psi(3770)$' sample of $2.93\,\mathrm{fb}^{-1}$ at $E_{\mathrm{cm}} = 3.773\,\mathrm{GeV}$, an '$XYZ$-scan' sample of $50.54\,\mathrm{pb}^{-1}$ at $E_{\mathrm{cm}} = 3.810\,\mathrm{GeV}$, and an '$R$-scan' sample of $7.95\,\mathrm{pb}^{-1}$ at $E_{\mathrm{cm}} = 3.850\,\mathrm{GeV}$. The first of these was analyzed by Derrick Toth with a separate procedure using double-tag reconstruction (both D and $\overline{D}$ in a single event). The other two samples were analyzed using the same procedure as for the scan data (See Sections 5.3 to 5.5). None of these points are used to determine the final results, as the differences between samples introduce additional systematics which overshadow any statistical improvement. However, these provide useful comparisons at important energy points along the cross section shape.

5.2.2 Luminosity Calculation

The integrated luminosity for each run is calculated following the procedure described in Ref. [30]. For each run, 1.4×10^6 $e^+e^- \rightarrow e^+e^-(\gamma)$ events were generated using Babayaga 3.5. We then select events with only two (oppositely) charged tracks, satisfying the event selection criteria $V_{xy} < 1$ cm, $|V_z| < 5$ cm, and $|\cos\theta| < 0.8$. After this, we accept only tracks that satisfy $E_{\text{EMC}} > 0.73 \times E_{\text{beam}}$ (cuts on $e^+e^- \rightarrow \mu^+\mu^-(\gamma)$ events) and $p > 0.93 \times E_{\text{beam}}$ (cuts on $e^+e^- \rightarrow \gamma J/\psi$, $J/\psi \rightarrow e^+e^-$ events). Applying these cuts to both data and MC identically, we use the resulting number of events found in the MC divided by the total generated to determine the efficiency (ϵ_{MC}). From this, and using the cross section provided by the generator (σ_{BB}), we can take the events found in data (N_{data}) to determine the integrated luminosity ($\mathcal{L}$) of each run:

$$\mathcal{L} = \frac{N_{\text{data}}}{\sigma_{BB}\ \epsilon_{MC}} \tag{5.5}$$

The integrated luminosity for each bin is shown in Table 5.1. The total luminosity for the data used is $(70.05 \pm 0.03)\,\text{pb}^{-1}$, where the error listed is statistical.

5.2.3 Monte Carlo Generation

To compare to the scan data sample, several Monte Carlo (MC) samples were produced. For the main signal determination, samples of generic $D^0\overline{D^0}$ from $\psi(3770)$ and generic D^+D^- from $\psi(3770)$ were generated with 10^5 events per run. In addition, $100\times$ data-size samples were produced for $q\bar{q}$, $\tau^-\tau^+$, radiative return to J/ψ (denoted $\gamma J/\psi$), and radiative return to $\psi(2S)$ (denoted $\gamma\psi'$). Each of these samples was generated at the University of Minnesota in July of 2014 using BOSS 6.6.4.p02. The $D^0\overline{D^0}$, D^+D^-, $q\bar{q}$, and $\tau^-\tau^+$ states were generated using KKMC, while the $\gamma J/\psi$ and $\gamma\psi'$ were generated with BesEvtGen. All except $q\bar{q}$ were then decayed with BesEvtGen. The total numbers of events in each sample can be found in Table 5.2.

 In general, all MC samples were generated based off communal decay card information used within BESIII. However, the $D\overline{D}$ samples were generated by implementing the Born-level cross section shape from the final fit into KKMC. This procedure was repeated over four iterations in order to provide a more data-driven basis for the ISR corrections. The effects of this process are examined in Section 5.6.

Bin	E_{cm} Range [GeV]	$\mathcal{L}$ [pb^{-1}]
0	3.735 - 3.736	0.3357(21)
1	3.736 - 3.737	0.4940(25)
2	3.737 - 3.744	0.3310(21)
3	3.744 - 3.746	0.9626(35)
4	3.746 - 3.748	1.4260(43)
5	3.748 - 3.750	2.2782(54)
6	3.750 - 3.752	2.9970(63)
7	3.752 - 3.754	3.3362(66)
8	3.754 - 3.755	3.4380(67)
9	3.755 - 3.758	3.8841(71)
10	3.758 - 3.761	4.4496(76)
11	3.761 - 3.764	4.4984(77)
12	3.764 - 3.767	3.2856(66)
13	3.767 - 3.770	2.4478(57)
14	3.770 - 3.773	2.0184(52)
15	3.773 - 3.776	1.8294(49)
16	3.776 - 3.779	1.8252(49)
17	3.779 - 3.782	1.9547(51)
18	3.782 - 3.785	2.1555(53)
19	3.785 - 3.788	2.5510(58)
20	3.788 - 3.792	2.8330(61)
21	3.792 - 3.796	3.5342(69)
22	3.796 - 3.800	4.0536(73)
23	3.800 - 3.803	3.9381(73)
24	3.803 - 3.806	2.7087(60)
25	3.806 - 3.809	1.7671(49)
26	3.809 - 3.812	1.2619(41)
27	3.812 - 3.815	0.9019(35)
28	3.815 - 3.823	0.6846(30)
29	3.823 - 3.830	0.4016(23)
30	3.830 - 3.839	0.2851(20)
31	3.839 - 3.847	0.2804(20)
32	3.847 - 3.855	0.2774(19)
33	3.855 - 3.863	0.3192(21)
34	3.863 - 3.870	0.3001(20)

Table 5.1: Measured luminosities for each energy bin.
The uncertainties listed are statistical errors from the data selection, as uncertainties from the MC statistics are negligible.

Sample	Number of Events
$\psi(3770) \rightarrow D^0\overline{D^0}$	1.660×10^7
$\psi(3770) \rightarrow D^+D^-$	1.620×10^7
$q\bar{q}$	8.916×10^7
$\gamma J/\psi$	7.307×10^6
$\gamma\psi'$	2.457×10^7
$\tau^-\tau^+$	2.164×10^7
Data	4.844×10^8

Table 5.2: Number of events contained in each generated sample and the scan data.

5.2.4 Software Packages

5.3 Signal Determination

We measure the yields of both $D^0\overline{D^0}$ and D^+D^- events with two-dimensional fits to ΔE and m_{BC}. MC samples are partitioned into the following four groups: proper D-tags ($N_{D\overline{D}}$), misreconstructed D-tags (N_{misrec}), continuum ($N_{q\bar{q}}$), and other (N_{other}). The first two groups are obtained using truth information from the $D\overline{D}$ samples, while the last group is a combination of the $\tau^-\tau^+$, $\gamma J/\psi$, and $\gamma\psi'$ samples. These groups are fitted to data using the RooFit package to perform a negative log-likelihood minimization for each energy bin (E_i) separately for both D^0 and D^+. For each fit, the four MC sample groups are used to construct 2D (ΔE vs. m_{BC}) PDF functions that are fitted against the corresponding data histograms. The proper $D\overline{D}$ shape is treated as signal, and its integral after fitting (N_D) is used for determining the signal yields and cross sections. An example fit is shown in Fig. 5.1, while the complete set of these plots can be found in Appendices B and C.

5.4 Efficiency Correction

In addition to the parameters gathered by DTagAlg, truth information was taken from the generic $D\overline{D}$ samples in order to determine the mode-by-mode reconstruction efficiency. To be deemed proper, a reconstruction must pass not only the standard D-tag cuts, but also match the generator information for the event. This process removes peaking backgrounds from modes with similar constituents. The total number of proper
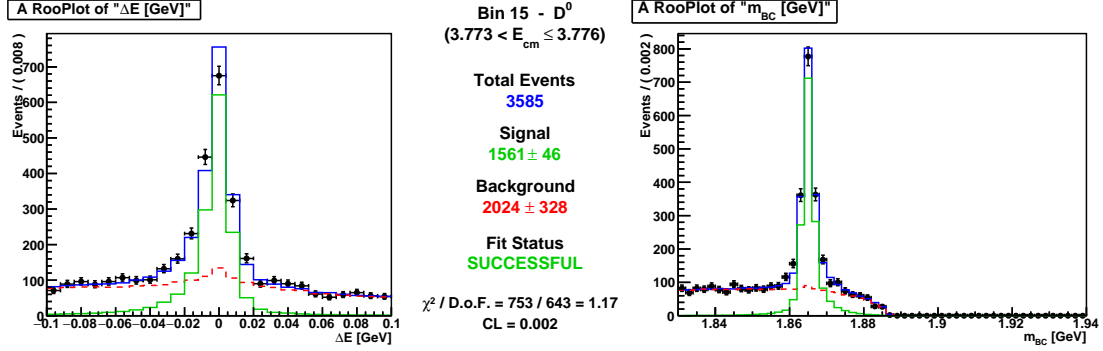
Figure 5.1: An example 2D signal fit.
The covers D^0 events in the region $3.773\,\text{GeV} < E_\text{cm} \leq 3.776\,\text{GeV}$. The data points (black) are fitted by the total MC shape (blue), which is the sum of the signal (green) and background (red) components.

D-tag reconstructions is then divided by the number of D particles generated for each mode, and the mode-by-mode efficiencies are weighted by the PDG branching ratios [1] to determine the overall efficiency (ϵ_D) for each of D^0 and D^+:

$$\epsilon_D = \sum_i \epsilon_i\, \mathcal{B}_i = \sum_i \left(\frac{N_{i\ \text{proper}}}{N_{i\ \text{generated}}} \right) \mathcal{B}_i. \tag{5.6}$$

Each D^0 efficiency also includes the corresponding DCSD terms for its decay (See Section 4.3).

To determine the cross section at each point, this procedure was applied separately for each energy bin. The total number of proper and generated particles for each energy bin are shown in Table 5.3 for D^0 and Tables 5.4 and 5.5 for D^+. The efficiencies for D^+ and D^0 were also calculated across the total sample, and are shown for each mode in Table 5.6 and Figure 5.2. Each energy bin's total efficiency for both D^0 and D^+ is shown in Table 5.7.

5.4.1   CP Violation Correction

Due to CP violation in the $D^0\overline{D^0}$ system, each of the neutral decay modes must be corrected to account for quantum correlations. This is done by applying scaling factors to the efficiency for each of the three modes used in reconstruction. The corrections are

Bin	$D^0 \to K^- \pi^+$		$D^0 \to K^- \pi^+ \pi^0$		$D^0 \to K^- \pi^+ \pi^+ \pi^-$	
	N_{prop}	N_{gen}	N_{prop}	N_{gen}	N_{prop}	N_{gen}
0	5519	7658	10757	27894	6927	16948
1	11203	15778	21753	56203	13704	33428
2	5470	7686	10761	27725	6929	16962
3	10987	15550	21357	55223	13639	33704
4	16311	23268	31913	83399	19997	50031
5	27586	38880	53505	138886	33927	83498
6	49416	69908	95785	250493	60813	150614
7	43530	62064	85248	222230	54013	134237
8	49056	70191	95402	250020	61035	150852
9	38764	54791	75237	194185	48307	116868
10	55219	77765	107785	277958	69525	167368
11	55412	78328	108229	278765	68944	167385
12	38502	54639	75111	194082	48743	117181
13	32802	46683	64440	166338	41593	100543
14	21886	30983	43041	111230	27326	66506
15	21849	31151	42979	110746	27406	66800
16	16534	23429	31906	83165	20645	50035
17	21963	31442	42724	110981	27807	67080
18	27328	38791	53480	139055	34434	83489
19	27019	38726	53396	139091	34605	83915
20	38332	54586	75296	194835	47966	117143
21	38032	54321	74841	195177	47764	117511
22	43289	62110	84373	222186	53400	133871
23	48974	70058	93686	249998	58965	150580
24	32426	46536	62154	166927	38264	99797
25	27022	38674	51590	138723	31748	83715
26	16588	23491	30978	83656	19168	50246
27	10832	15519	20060	55573	12281	33523
28	10651	15284	20306	55439	12505	33815
29	10980	15661	20233	55701	12405	33649
30	5398	7822	9954	27637	6060	16711
31	5425	7804	10010	27618	6156	16729
32	5439	7830	10009	27799	5988	16695
33	10659	15442	20070	55385	12282	33515
34	10615	15443	19910	55573	12345	33592

Table 5.3: Number of proper and generated particles for D^0.
The mode-by-mode numbers of particles used in the efficiency calculations for
$D^0 \to K^- \pi^+, D^0 \to K^- \pi^+ \pi^0$, and $D^0 \to K^- \pi^+ \pi^+ \pi^-$.

Bin	$D^+ \to K^- \pi^+ \pi^+$		$D^+ \to K^- \pi^+ \pi^+ \pi^0$		$D^+ \to K_S^0 \pi^+$	
	N_{prop}	N_{gen}	N_{prop}	N_{gen}	N_{prop}	N_{gen}
3	20022	37668	6600	24160	2272	5902
4	30234	56234	10010	36416	3431	8931
5	50966	93874	16855	60686	5750	14833
6	91414	169401	29807	109330	10199	26677
7	81267	150434	26528	96948	9060	23797
8	90448	168761	30206	109641	10233	26927
9	71896	131281	23901	85264	8167	20918
10	103179	187949	34092	121352	11695	29969
11	103605	188336	34331	122120	11672	29828
12	72921	132064	23962	84947	8199	20937
13	62056	112433	20547	72991	7021	17781
14	41328	75280	13636	48338	4739	11979
15	41441	75211	13640	48504	4613	11861
16	31212	56487	10309	36655	3513	8982
17	41621	75045	13881	49145	4680	12048
18	51909	94077	16905	60819	5769	14879
19	52042	94156	17035	60618	5885	14977
20	72086	131300	23647	84907	8286	21035
21	72509	131694	23555	84570	8029	20806
22	82597	150805	26792	96787	9334	23503
23	92228	169069	29808	109702	10559	26985
24	61616	113123	19611	73321	6985	18018
25	50613	93767	16383	60811	5712	14759
26	30736	56653	9583	36280	3614	9245
27	20427	37582	6456	24186	2250	5811
28	20295	37687	6536	24289	2214	5811
29	20393	37337	6489	24201	2466	6167
30	10309	18737	3128	12099	1159	3003
31	10345	18895	3216	12023	1120	2946
32	10142	18893	3213	12066	1168	3020
33	20265	37114	6374	24194	2330	5967
34	20311	37337	6362	24378	2326	6057

Table 5.4: Number of proper and generated particles for D^+ (part 1). The mode-by-mode numbers of particles used in the efficiency calculations for $D^+ \to K^- \pi^+ \pi^+, D^+ \to K^- \pi^+ \pi^+ \pi^0$, and $D^+ \to K_S^0 \pi^+$.

Bin	$D^+ \to K_S^0 \pi^+ \pi^0$		$D^+ \to K_S^0 \pi^+ \pi^+ \pi^-$		$D^+ \to K^+ K^- \pi^+$	
	N_{prop}	N_{gen}	N_{prop}	N_{gen}	N_{prop}	N_{gen}
3	5578	27502	3414	14899	1698	3980
4	8468	41353	4999	22340	2485	5867
5	14556	69102	8309	37104	4344	9959
6	25432	124123	14807	66943	7430	17744
7	22850	110296	13319	60059	6723	15843
8	25820	124151	15057	66954	7478	17655
9	20373	96362	11898	52068	6093	13955
10	29030	138372	17076	74519	8425	19594
11	29195	137508	17221	74539	8534	19799
12	20216	96603	12006	52123	5985	13833
13	17507	82589	10228	44534	5111	11746
14	11705	54998	6839	29643	3429	7891
15	11602	55245	6810	29770	3461	7989
16	8763	41572	4963	22250	2564	5876
17	11651	55576	6953	29754	3341	7827
18	14509	68677	8617	37138	4235	9867
19	14565	68864	8466	36828	4361	9826
20	20572	97073	12192	52476	6187	13850
21	20411	96827	11748	52152	5898	13671
22	23090	109958	13325	59244	6906	15913
23	25746	124249	14667	66799	7601	17652
24	17179	82921	9571	44714	4994	11729
25	14120	69390	7922	37132	4165	9905
26	8380	41424	4794	22343	2562	5908
27	5593	27680	3072	14738	1694	3935
28	5627	27587	3151	14791	1657	3859
29	5677	27727	3118	14862	1700	3924
30	2863	13875	1604	7514	849	2003
31	2733	13650	1554	7495	828	1971
32	2808	13903	1491	7273	876	2005
33	5572	27708	3168	14898	1659	3890
34	5627	27755	3095	14821	1692	3962

Table 5.5: Number of proper and generated particles for D^+ (part 2). The mode-by-mode numbers of particles used in the efficiency calculations for $D^+ \to K_S^0 \pi^+ \pi^0, D^+ \to K_S^0 \pi^+ \pi^+ \pi^-$, and $D^+ \to K^+ K^- \pi^+$.

Decay Mode (i)	PDG $\mathcal{B}_i$ [%]	MC Efficiency ϵ_i
$D^0 \to K^- \pi^+$	3.89 ± 0.05	$0.70226(74)$
$D^0 \to K^- \pi^+ \pi^0$	13.93 ± 0.50	$0.38190(29)$
$D^0 \to K^- \pi^+ \pi^+ \pi^-$	8.11 ± 0.20	$0.40277(38)$
$\epsilon_{D^0} = (11.320 \pm 0.213)\%$		
$D^+ \to K^- \pi^+ \pi^+$	9.13 ± 0.19	$0.54699(42)$
$D^+ \to K^- \pi^+ \pi^+ \pi^0$	5.99 ± 0.18	$0.27570(38)$
$D^+ \to K^0_S \pi^+$	1.47 ± 0.07	$0.38972(89)$
$D^+ \to K^0_S \pi^+ \pi^0$	6.99 ± 0.27	$0.20864(31)$
$D^+ \to K^0_S \pi^+ \pi^+ \pi^-$	3.12 ± 0.11	$0.22540(43)$
$D^+ \to K^+ K^- \pi^+$	0.95 ± 0.03	$0.43199(116)$
$\epsilon_{D^+} = (9.792 \pm 0.134)\%$		

Table 5.6: Mode-by-mode reconstruction efficiencies for D^0 and D^+.
The values shown are over the entire data sample, while calculations for the cross
sections use the values of each energy point individually.

parameterized for each mode (m) by the following form [31]:

$$\alpha_{D^0 \to m} = 1 + r_m^2 + 2 \times y \times r_m \times R_m \times \cos(\delta_m). \tag{5.7}$$

Here, r_m and δ_m represent the relative magnitudes and phases between the Cabbibo-favored and doubly-Cabbibo-suppressed modes, respectively, while the factor of R_m represents a coherence factor characterizing the variation of δ_m over phase space. Note, there is no such variation for a two-body decay (like $D^0 \to K^- \pi^+$), so $R_{D^0 \to K^- \pi^+} = 1$. The value of y represents the difference in total width components of the $D^0 \overline{D^0}$ system, $y = (\Gamma_2 - \Gamma_1)/(\Gamma_2 + \Gamma_1)$, where 1 and 2 represent the CP-odd and CP-even states, respectively.

The mode-dependent values for these factors are listed in Table 5.8. These are taken from the CPV-allowed values in [32] for $D^0 \to K^- \pi^+$, and from [33] for $D^0 \to K^- \pi^+ \pi^0$ and $D^0 \to K^- \pi^+ \pi^+ \pi^-$. The value of $y = 0.0066^{+0.0007}_{-0.0010}$ is also from [32], and is the same for all modes. After applying each of the mode-dependent corrections, the efficiency for the full sample changes from $\epsilon_{D^0} = (11.320 \pm 0.213)\%$ to $\epsilon_{D^0} = (11.352 \pm 0.213)\%$, and similarly for the efficiencies of each E_{cm} bin.

E_{bin}	ϵ_{D^0}	ϵ_{D^+}
0	0.1149 ± 0.0023	-
1	0.1148 ± 0.0022	-
2	0.1149 ± 0.0023	-
3	0.1142 ± 0.0022	0.0959 ± 0.0014
4	0.1130 ± 0.0022	0.0965 ± 0.0014
5	0.1142 ± 0.0022	0.0978 ± 0.0014
6	0.1135 ± 0.0021	0.0964 ± 0.0013
7	0.1134 ± 0.0021	0.0968 ± 0.0013
8	0.1132 ± 0.0021	0.0966 ± 0.0013
9	0.1150 ± 0.0022	0.0986 ± 0.0014
10	0.1153 ± 0.0022	0.0986 ± 0.0014
11	0.1150 ± 0.0022	0.0990 ± 0.0014
12	0.1151 ± 0.0022	0.0990 ± 0.0014
13	0.1149 ± 0.0022	0.0992 ± 0.0014
14	0.1147 ± 0.0022	0.0991 ± 0.0014
15	0.1146 ± 0.0022	0.0988 ± 0.0014
16	0.1144 ± 0.0022	0.0989 ± 0.0014
17	0.1144 ± 0.0022	0.0993 ± 0.0014
18	0.1144 ± 0.0022	0.0988 ± 0.0014
19	0.1141 ± 0.0022	0.0993 ± 0.0014
20	0.1144 ± 0.0022	0.0989 ± 0.0014
21	0.1136 ± 0.0022	0.0985 ± 0.0014
22	0.1124 ± 0.0021	0.0983 ± 0.0014
23	0.1112 ± 0.0021	0.0973 ± 0.0014
24	0.1101 ± 0.0021	0.0967 ± 0.0014
25	0.1098 ± 0.0021	0.0960 ± 0.0014
26	0.1100 ± 0.0021	0.0961 ± 0.0014
27	0.1072 ± 0.0021	0.0960 ± 0.0014
28	0.1081 ± 0.0021	0.0959 ± 0.0014
29	0.1078 ± 0.0021	0.0968 ± 0.0014
30	0.1064 ± 0.0021	0.0965 ± 0.0015
31	0.1074 ± 0.0021	0.0961 ± 0.0015
32	0.1063 ± 0.0021	0.0953 ± 0.0015
33	0.1071 ± 0.0021	0.0961 ± 0.0014
34	0.1065 ± 0.0021	0.0957 ± 0.0014

Table 5.7: The overall reconstruction efficiency of D^0 and D^+ for each energy bin. These values are used to calculate the corresponding cross sections at each energy point. The listed errors are statistical only.
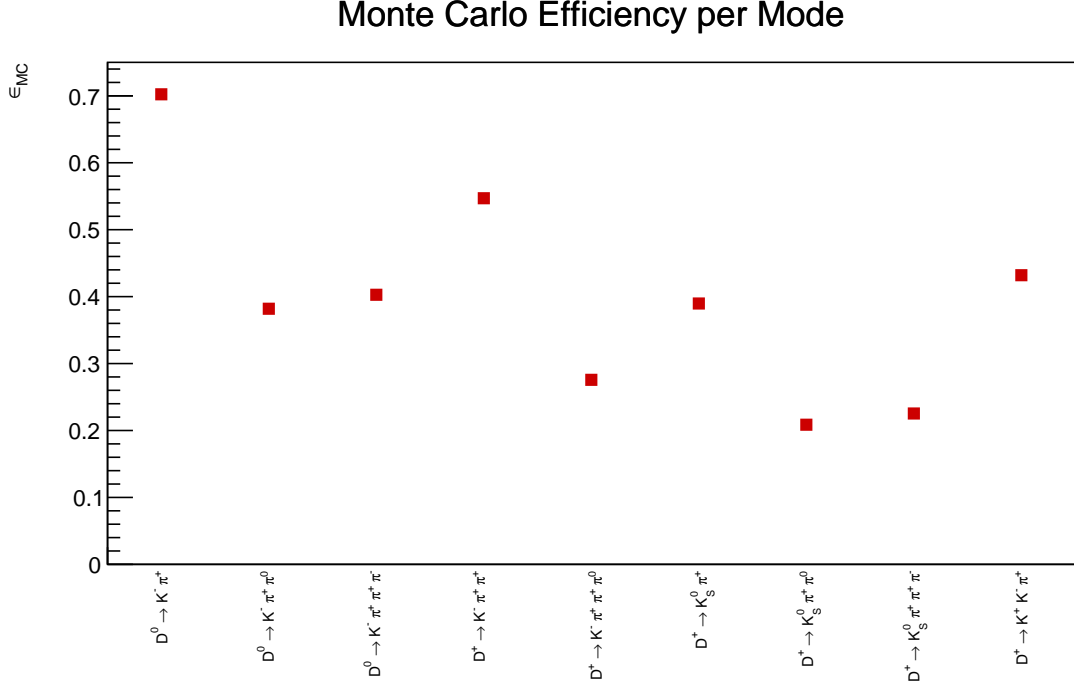
Figure 5.2: Mode-by-mode MC efficiencies for D^0 and D^+.
The error bars are negligible on the scale shown.

5.5 Fitting Procedure

After applying the correction in Section 5.4.1, the efficiency values (Table 5.7) were combined with the luminosity (Table 5.1) and the signal values from each 2D fit (Table 5.9) to determine the cross section at each energy point. Since each $\psi(3770)$ produces a $D\overline{D}$ pair, a factor of 2 is included to avoid double counting:

$$\sigma_{D\overline{D}}^{RC}(E_i) = \frac{N_D(E_i)}{2\,\epsilon_D(E_i)\,\mathcal{L}(E_i)}. \tag{5.8}$$

The resulting cross section values for D^0 and D^+ are also listed in Table 5.9, and shown in Figure 5.3.

Using the measured $D\overline{D}$ cross sections, we fit to Equation (2.7) using each of the form factor choices described in Section 5.1. In each case, there are four common fit parameters: $M^{\psi(3770)}$, $\Gamma^{\psi(3770)}$, $\Gamma_{ee}^{\psi(3770)}$, and $\phi^{\psi(3770)}$. These represent the mass, total

Mode	r_m	R_m	δ_m [°]	α_m
$D^0 \to K^- \pi^+$	0.0591 ± 0.0063	1	$11.8 \; ^{+ \; 9.5}_{- \; 14.7}$	1.00426 ± 0.00083
$D^0 \to K^- \pi^+ \pi^0$	0.0447 ± 0.0012	0.81 ± 0.06	$18 \; ^{+ \; 14}_{- \; 15}$	1.00248 ± 0.00014
$D^0 \to K^- \pi^+ \pi^+ \pi^-$	0.0549 ± 0.0006	$0.43 \; ^{+ \; 0.17}_{- \; 0.13}$	$-52 \; ^{+ \; 28}_{- \; 17}$	$1.00270 \; ^{+ \; 0.00014}_{- \; 0.00012}$

Table 5.8: The quantum correlated factors for the D^0 modes.
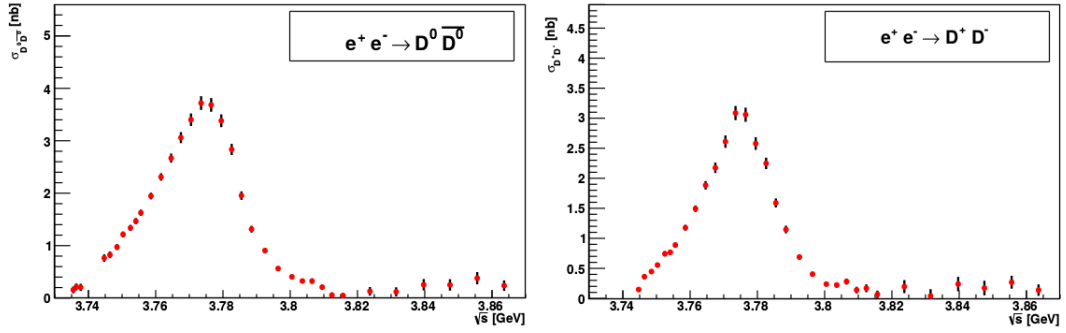
Figure 5.3: The measured $e^+ e^- \to D\overline{D}$ cross sections.
The $D^0 \overline{D^0}$ cross section is shown on the left and $D^+ D^-$ is shown on the right.

width, electron partial width, and relative phase to the non-resonant contribution for the $\psi(3770)$, respectively. This notation for the total width corresponds to $\Gamma(M)$ in Section 2.3. Two additional fitting parameters are dependent on which form factor is being used: F_{NR} and a_{NR} for the exponential, or $\Gamma^{\psi(2S)}$ and F_0 for the VDM. For the former, these represent the amplitude and exponent normalization for the non-resonant contribution. In the latter case, these represent the modified total width for the $\psi(2S)$ above resonance (see Section 5.1) and the constant contribution of resonances above the $\psi(3770)$. The fitting is done simultaneously for D^0 and D^+ with identical parameters using TMinuit with a χ^2 minimization. The value minimized is the sum of the χ^2 values from each of the D^0 and D^+ cross section functions. Results for the Exponential and VDM choices are shown in Figures 5.4 and 5.5, respectively.

E_{mid}	$N_{D^0\overline{D^0}}$	$\sigma^{RC}_{D^0\overline{D^0}}$ [nb]	$N_{D^+D^-}$	$\sigma^{RC}_{D^+D^-}$ [nb]
3.7355	12 ± 5	0.155 ± 0.065	-	-
3.7364	24 ± 7	0.212 ± 0.066	-	-
3.7377	15 ± 5	0.204 ± 0.069	-	-
3.7447	166 ± 15	0.761 ± 0.072	27 ± 6	0.147 ± 0.038
3.7464	266 ± 20	0.823 ± 0.064	98 ± 12	0.361 ± 0.046
3.7485	508 ± 27	0.970 ± 0.056	199 ± 17	0.446 ± 0.040
3.7503	825 ± 34	1.210 ± 0.055	321 ± 22	0.555 ± 0.039
3.7525	1012 ± 38	1.334 ± 0.057	479 ± 27	0.743 ± 0.043
3.7541	1143 ± 41	1.462 ± 0.059	510 ± 28	0.767 ± 0.044
3.7556	1454 ± 45	1.622 ± 0.059	680 ± 32	0.887 ± 0.044
3.7586	1993 ± 53	1.940 ± 0.064	1036 ± 39	1.177 ± 0.048
3.7616	2388 ± 58	2.303 ± 0.071	1323 ± 44	1.493 ± 0.054
3.7646	2016 ± 53	2.662 ± 0.086	1224 ± 42	1.884 ± 0.070
3.7675	1719 ± 48	3.051 ± 0.104	1050 ± 38	2.174 ± 0.086
3.7705	1578 ± 46	3.391 ± 0.119	1044 ± 38	2.610 ± 0.103
3.7735	1561 ± 46	3.708 ± 0.131	1116 ± 39	3.086 ± 0.118
3.7765	1543 ± 45	3.673 ± 0.130	1108 ± 39	3.058 ± 0.118
3.7795	1522 ± 46	3.372 ± 0.121	1001 ± 38	2.579 ± 0.105
3.7826	1398 ± 44	2.826 ± 0.106	957 ± 38	2.248 ± 0.095
3.7855	1140 ± 41	1.948 ± 0.080	806 ± 36	1.589 ± 0.075
3.7885	848 ± 38	1.310 ± 0.064	645 ± 34	1.147 ± 0.064
3.7925	725 ± 37	0.903 ± 0.050	480 ± 30	0.688 ± 0.045
3.7964	514 ± 35	0.561 ± 0.040	321 ± 31	0.403 ± 0.040
3.8005	354 ± 31	0.404 ± 0.037	182 ± 28	0.238 ± 0.037
3.8036	194 ± 23	0.324 ± 0.039	117 ± 22	0.223 ± 0.043
3.8065	125 ± 19	0.323 ± 0.050	95 ± 16	0.280 ± 0.050
3.8095	57 ± 13	0.206 ± 0.048	33 ± 13	0.138 ± 0.055
3.8124	11 ± 9	0.056 ± 0.050	29 ± 11	0.168 ± 0.065
3.8157	6 ± 7	0.046 ± 0.050	8 ± 8	0.067 ± 0.062
3.8237	11 ± 7	0.128 ± 0.081	15 ± 8	0.196 ± 0.108
3.8315	7 ± 5	0.118 ± 0.086	2 ± 6	0.039 ± 0.114
3.8397	15 ± 6	0.254 ± 0.108	12 ± 6	0.239 ± 0.119
3.8475	14 ± 6	0.250 ± 0.109	9 ± 6	0.172 ± 0.121
3.8556	26 ± 8	0.377 ± 0.117	16 ± 6	0.269 ± 0.108
3.8636	15 ± 6	0.236 ± 0.099	7 ± 5	0.138 ± 0.095

Table 5.9: The $D\overline{D}$ cross section at each E_{cm} point.
The number of data events observed in each E_{cm} bin are also shown. The uncertainties on the cross sections are statistical only and come from the signal fitting (N_D), PDG values (Table 5.6), and MC reconstruction efficiency (Table 5.7). The values for $N_{D^0\overline{D^0}}$ and $N_{D^+D^-}$ are taken from the signal fits shown in Appendices B and C.
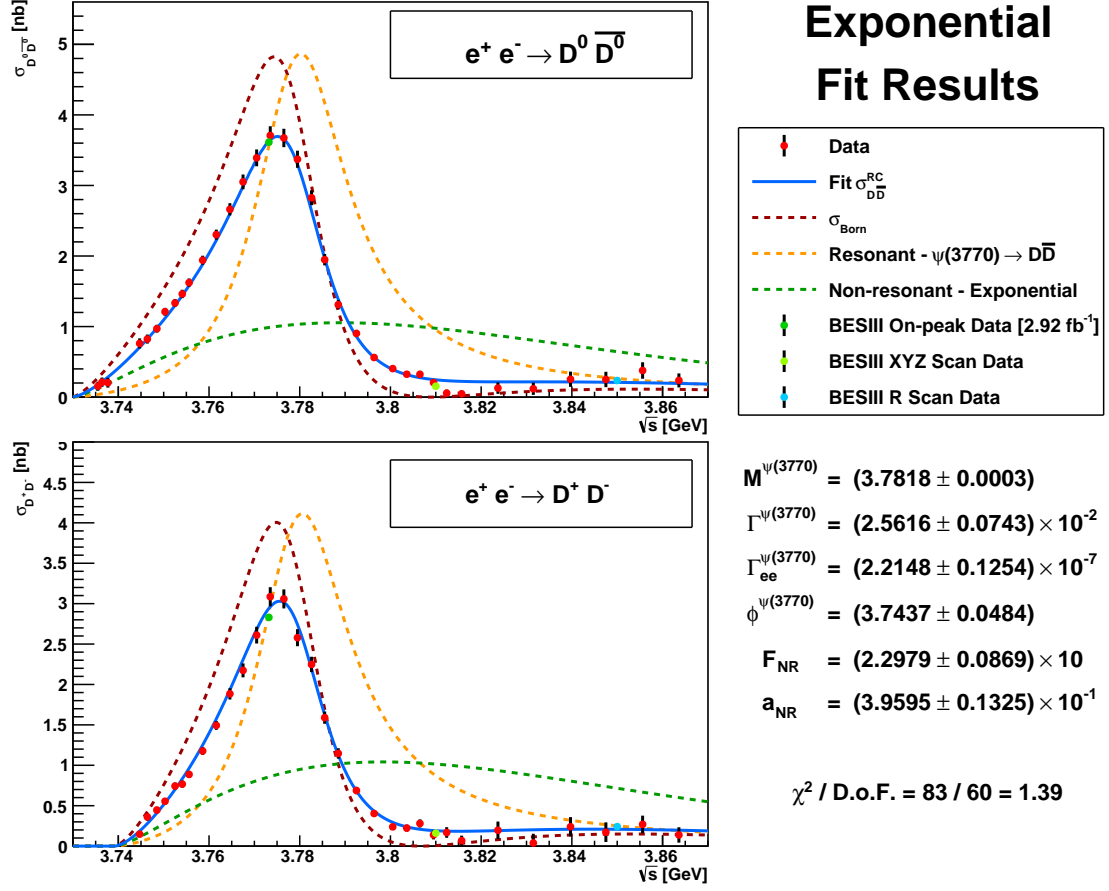
Figure 5.4: The Exponential Model fit results.
The results for D^0 are shown on the top and the results for D^+ are shown on the bottom. The fit shape (blue) is calculated from Equation (2.1) using the non-resonant component from Equation (5.2).

5.5.1 Coulomb Correction

In the development of this analysis, it was discovered that the theoretical formulation in Section 2.3 did not lead to a successful fit of the $D\overline{D}$ cross sections, shown in Figure 5.6. Namely, including the Coulomb effect pulls the $D^0\overline{D^0}$ and D^+D^- cross sections in opposite directions. We found the best fits were achieved by altering Equation (2.3) to set the Coulomb factor to 1. While this disagrees with conventional theoretical wisdom, it is consistent with studies of $\Upsilon(4S) \to B\overline{B}$ where applying a Coulomb correction for
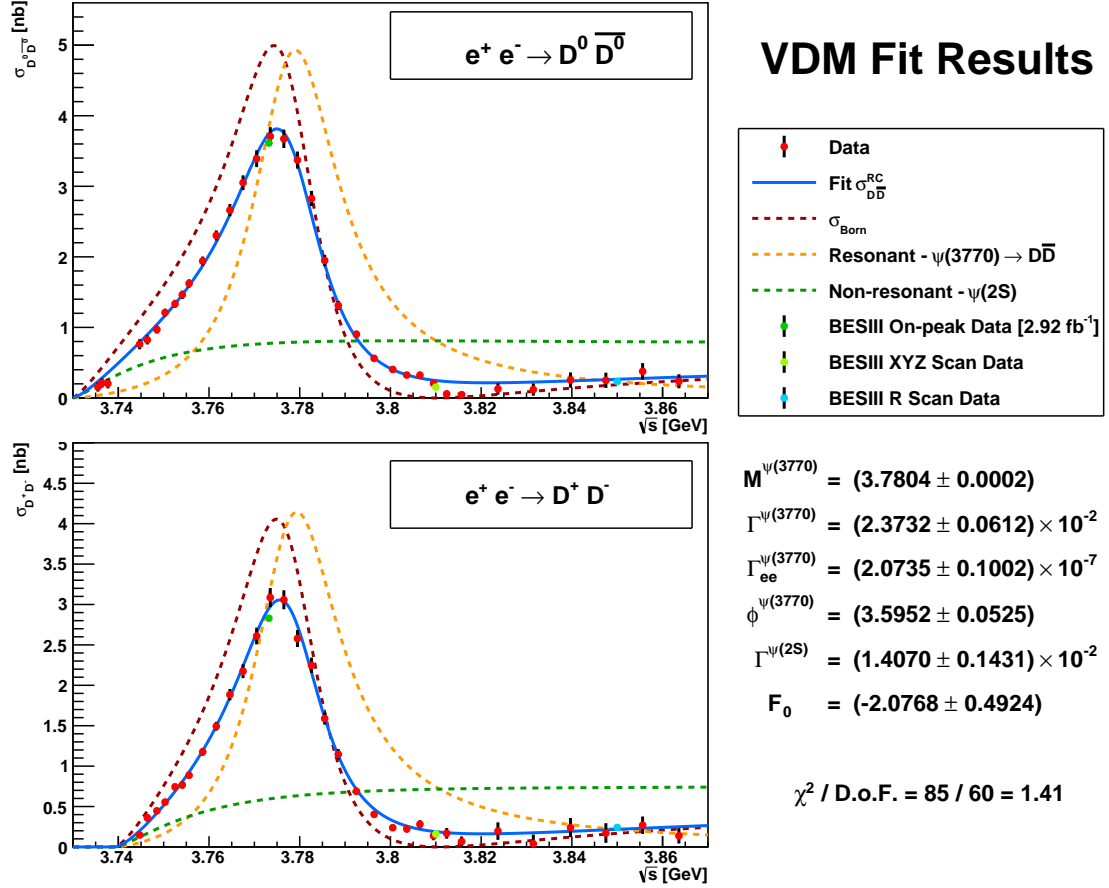
Figure 5.5: The Vector Dominance Model fit results.
The results for D^0 are shown on the top and the results for D^+ are shown on the bottom. The fit shape (blue) is calculated from Equation (2.1) using the non-resonant component from Equation (5.3).

the charged final state also leads to inconsistency with data.

This is most clearly seen in the ratio of D^+D^- and $D^0\overline{D^0}$ cross sections, shown in Figure 5.7, where the 'No Coulomb' method sets $z_{D^+D^-}$ in Equations (2.7) and (2.11) to unity, the 'Partial Coulomb' sets this factor to unity only for Equation (2.7), and the 'Full Coulomb' is the default assumption. Agreement of the measured cross section ratio with the 'No Coulomb' calculation is substantially better. This is also true for the high statistics points measured at the $\psi(3770)$ peak by Derrick Toth [?] (light blue). As the data tend to follow the 'No Coulomb' method, we choose this as our nominal method for the results, presented in Section 5.7. However, the interpretation for this behavior is still undetermined.

5.6 Systematics

To assess the systematic uncertainties in our results, we look at a variety of factors. Many of these affect all BESIII analyses, such as luminosity and tracking. Others, like the modification to KKMC generation (see Section 5.2.3), are specific to this analysis. The remaining systematics are typically due to less well-known parameters, like the radii used to describe the $\psi(2S)$ and $\psi(3770)$ (see Section 5.1). Each of these contributions, as well as their total, can be found in ??.

Each systematic is obtained by changing a specific aspect, and re-fitting to the altered values using the VDM method. The uncertainties for each parameter are obtained by taking the difference between this result and the nominal fit (Figure 5.5). Generally, each change was done both positively and negatively, and the value used is the largest difference seen between the two changes. The contributing systematics are summarized below:

Luminosity

A 1 % change was applied to $\mathcal{L}$ in Equation (5.8).

$\pi^\pm/K^\pm$ Tracking

A 1.0 % change was applied for each $\pi^\pm$ or $K^\pm$ in a given decay mode. The summed contribution for each mode is applied to ϵ_m in Equation (5.6).
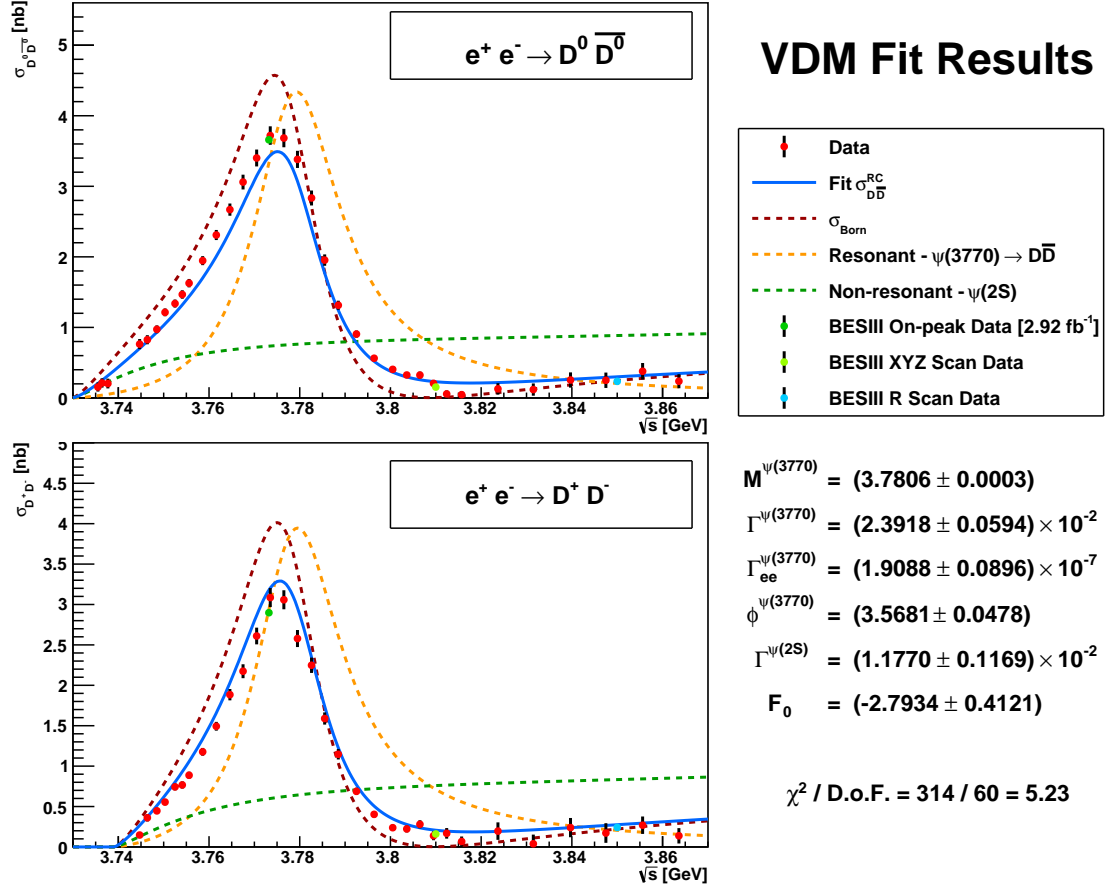
Figure 5.6: The Vector Dominance Model fit results with Coulomb interactions. The results for D^0 are shown on the top and the results for D^+ are shown on the bottom. Including this factor provides notably worse results than when excluding it (see Figure 5.5).
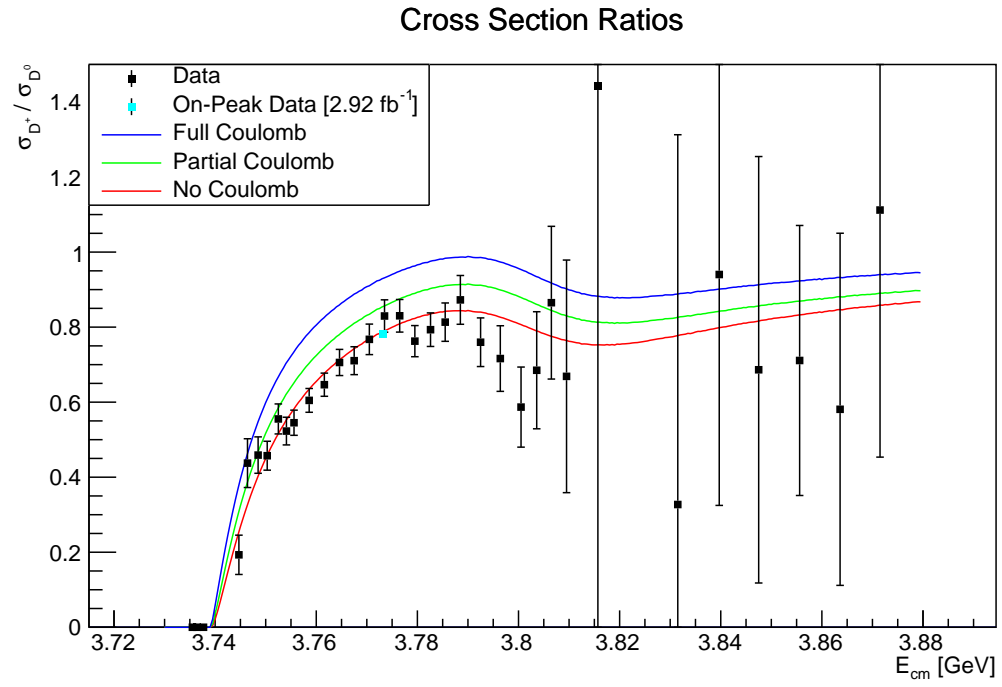
Figure 5.7: The ratio of D^+ to D^0 cross sections.
Several levels of Coulomb interactions are examined.

π^0 Tracking

A 2.0 % change was applied for each π^0 in a given decay mode. The summed contribution for each mode is applied to ϵ_m in Equation (5.6).

K_S^0 Tracking

A 1.5 % change was applied for each K_S^0 in a given decay mode. The summed contribution for each mode is applied to ϵ_m in Equation (5.6).

Signal Shape

A mode-dependent change was applied to N in Equation (5.8). Differences in signal shapes were obtained by Derrick Toth after examining the use of single-Gaussian convolved signal shapes, and are shown in Table 5.10. The changes applied were obtained from the sums of the mode-dependent values averaged over their branching fractions.

Tag Mode	Difference (%)
$D^0 \to K^- \pi^+$	0.27
$D^0 \to K^- \pi^+ \pi^0$	0.10
$D^0 \to K^- \pi^+ \pi^+ \pi^-$	0.47
D^0 Average: 0.24 %	
$D^+ \to K^- \pi^+ \pi^+$	0.20
$D^+ \to K^- \pi^+ \pi^+ \pi^0$	0.00
$D^+ \to K_S^0 \pi^+$	0.17
$D^+ \to K_S^0 \pi^+ \pi^0$	0.29
$D^+ \to K_S^0 \pi^+ \pi^+ \pi^-$	0.17
$D^+ \to K^+ K^- \pi^+$	0.74
D^+ Average: 0.19 %	

Table 5.10: Signal shape differences by mode.
The total D^0 and D^+ values are averaged over the branching fractions of each mode.

In generating the MC samples for this analysis, several used a modified form of KKMC which accounted for the line shape of the $\psi(3770)$. However, as this shape is also the final output of the procedure, only an estimation of the results can be used for generation. To assess the variation from the input shape, we compared the output fit

parameters to those used in the generation process, and found very similar fit parameters. This process used the Exponential method, and can be found in Table 5.11. The numbers listed are from an earlier iteration of the MC than shown in Sec. 5.5, but the consistency seen is representative of all iterations. Very little difference is seen in the primary fitting parameters of the $\psi(3770)$. These similarities show the fit result values converging, even after only a single iteration.

	$M^{\psi(3770)}$ [GeV]	$\Gamma^{\psi(3770)}$ [MeV]	$\Gamma_{ee}^{\psi(3770)\to D\overline{D}}$ [eV]	$\phi^{\psi(3770)}$	$\Gamma^{\psi(2S)}$ [MeV
Fit Results	3.7814 ± 0.0003	24.839 ± 0.681	214.65 ± 11.10	3.6375 ± 0.0518	20.147 ± 1.76
KKMC Input	3.7815 ± 0.0003	24.887 ± 0.686	217.55 ± 11.18	3.6374 ± 0.0513	21.394 ± 1.86

Table 5.11: The parameters used to modify the KKMC lineshape of the $\psi(3770)$ compared to the Exponential fit results.

We also considered an alternative MC simulation of the $D\overline{D}$ samples based on the ConExc generator in place of KKMC. This process used an input Born level shape identical to that used in the final iteration produced with KKMC. Each of the background samples used (such as $q\bar{q}$ and $\tau^-\tau^+$) were the same as in the nominal procedure. The cross section results using the VDM model are shown in Fig. 5.8, and provide $\psi(3770)$ fit parameters within the statistical errors of the nominal method, as seen in Fig. 5.5. From this, we treat variations due to the MC generation as negligible.

5.7   Results
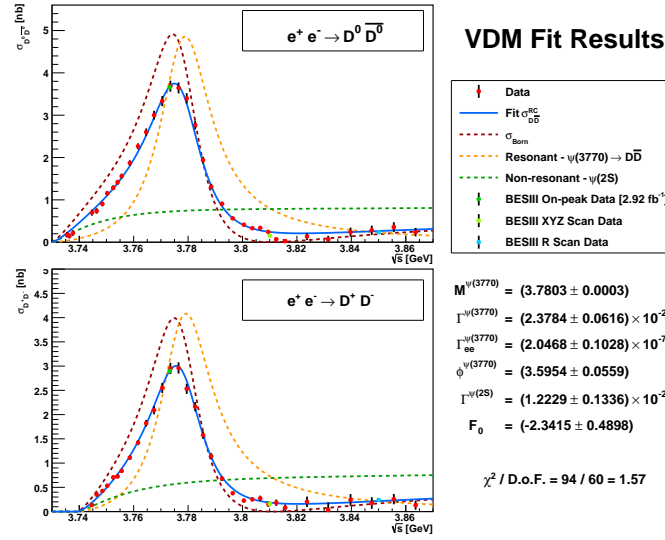
Figure 5.8: The Vector Dominance Model fit results for (left) D^0 and (right) D^+. The underlying MC shapes for the $D\overline{D}$ components were generated using ConExc instead of KKMC.

Chapter 6

Measurement of Hadronic Production and $\Gamma(\psi(3770) \to \text{non-}D\overline{D})$

6.1   Data and Monte Carlo Samples

6.2   Event Selection

6.3   Efficiency Extrapolation

6.4   Background Subtraction

6.5 $D\overline{D}$ Correction

6.6   Hadron Counting

6.7   Results

Chapter 7

Conclusion

This is where the Conclusions go!

References

[1] K.A. Olive et al. (Particle Data Group), Chin. Phys. C, **38**, 090001 (2014).

[2] J. L. Rosner, Phys. Rev. D **64**, 094002 (2001) [hep-ph/0105327].

[3] J. L. Rosner, Annals Phys. **319**, 1 (2005) [hep-ph/0411003].

[4] S. Okubo, Phys. Lett. **5**, 165 (1963).

[5] G. Zweig, Developments in the Quark Theory of Hadrons, Volume 1. Edited by D. Lichtenberg and S. Rosen. pp. 22-101

[6] J. Iizuka, K. Okada and O. Shito, Prog. Theor. Phys. **35**, 1061 (1966).

[7] E. A. Kuraev and V. S. Fadin, Sov. J. Nucl. Phys. **41**, 466 (1985) [Yad. Fiz. **41**, 733 (1985)].

[8] V. V. Anashin *et al.*, Phys. Lett. B **711**, 292 (2012) [arXiv:1109.4205 [hep-ex]].

[9] J. M. Blatt and V. F. Weisskopf, Theoretical Nuclear Physics, Wiley, New York, (1952).

[10] M. Ablikim *et al.* [BESIII Collaboration], Nucl. Instrum. Meth. A **614**, 345 (2010) [arXiv:0911.4960 [physics.ins-det]].

[11] J. D. Jackson. *Classical Electrodynamics (3rd ed.)*. Wiley. (Section 13.2)

[12] W. Li, *et al.*, Proc. Int. Conf. Comput. High Energy and Nucl. Phys. 225 (2006).

[13] See `http://linux.web.cern.ch/linux/scientific5`.

[14] G. Barrand, I. Belyaev, P. Binko, M. Cattaneo, R. Chytracek, G. Corti, M. Frank and G. Gracia *et al.*, Comput. Phys. Commun. **140**, 45 (2001).

[15] C. Arnault, "CMT: A software configuration management tool," (2000).

[16] See `http://root.cern.ch`.

[17] S. Agostinelli, *et al.*, Nucl. Instr. and Meth. **506**, (3), 250 (2003); J. Allison, *et al.*, IEEE Trans. Nucl. Sci. NS **53** (1), 270 (2006); See `http://www.geant4.org/geant4`.

[18] S. Jadach , B. F. L. Ward and Z. Was, Comp. Phys. Commun. **130**, 260 (2000); S. Jadach, B. F. L. Ward and Z. Was, Phys. Rev. D **63**, 113009 (2001).

[19] S. Jadach, Z. Was, R. Decker and J. H. Kuhn, Comput. Phys. Commun. **76**, 361 (1993).

[20] See `http://home.thep.lu.se/~torbjorn/Pythia.html`.

[21] D.J. Lange, Nucl. Instrum. Meth. A **462**, 152 (2001).

[22] R. G. Ping, Chinese Physics C **32**, 8 (2008).

[23] E. Barberio, B. van Eijk and Z. Was, Comput. Phys. Commun. **66**, 115 (1991).

[24] J. C. Chen, G. S. Huang, X. R. Qi, D. H. Zhang and Y. S. Zhu, Phys. Rev. D **62**, 034003 (2000).

[25] G. Bonneau and F. Martin, Nucl. Phys. B **27**, 381 (1971).

[26] C.M. Carloni Calame, G. Montagna, O. Nicrosini, F. Piccinini, Nucl. Phys. Proc. Suppl. **131** 48-55 (2004).

[27] See `http://www.mysql.com/about`.

[28] R. M. Baltrusaitis *et al.* [MARK-III Collaboration], Phys. Rev. Lett. **56**, 2140 (1986).

[29] J. Adler *et al.* [MARK-III Collaboration], Phys. Rev. Lett. **60**, 89 (1988).

[30] A. Hafner, "Luminosity Measurement for the $\psi(3770)$ data at BESIII," BESIII-doc-406-v2 (2015).

[31] D. M. Asner and W. M. Sun, Phys. Rev. D, **77**, 019901 (2008).

[32] HFAG 2015 (CPV-Allowed) [http://www.slac.stanford.edu/xorg/hfag/charm/CHARM15/results_mi

[33] T. Evans et al., Physics Letters B 757 (2016) 520527.

Appendix A

Glossary and Acronyms

Care has been taken in this thesis to minimize the use of jargon, but this cannot always be achieved. This appendix defines certain terms used in a glossary, and contains a table of acronyms and initialisms used along with their meanings.

A.1 Glossary

- **Cosmic-Ray Muon** (**CR** μ) – A muon coming from the abundant energetic particles originating outside of the Earth's atmosphere.

A.2 Acronyms / Initialisms

Table A.1: Acronyms and Initialisms

Name	Meaning
BESIII	The third Beijing Spectrometer
IHEP	Institute of High Energy Physics
BEPCII	The second Beijing Electron-Position Collider
MDC	Multi-Layer Drift Chamber
ToF	Time-of-Flight System
	Continued on next page

Table A.1 – Continued from previous page

Acronym	Meaning
EMC	Electromagnetic Calorimeter
MUC	Muon Identifier
PMTs	Photomultipler Tubes
RPC	Resistive Plate Counter
BOSS	BESIII Offline Software System
MC	Monte Carlo
ADC	Analog-to-Digital Conversion
TDC	Time-to-Digital Conversion

Appendix B

D^0 Signal Fits

Signal Fit - D^0 Bin 0
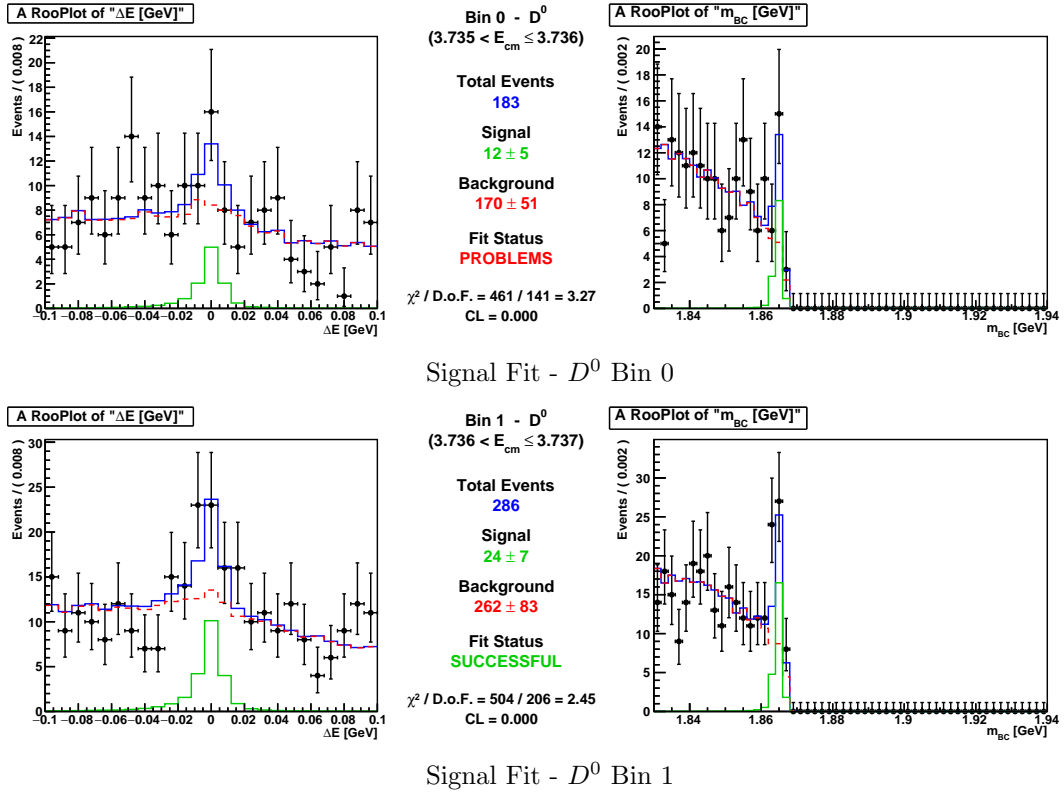
Signal Fit - D^0 Bin 1
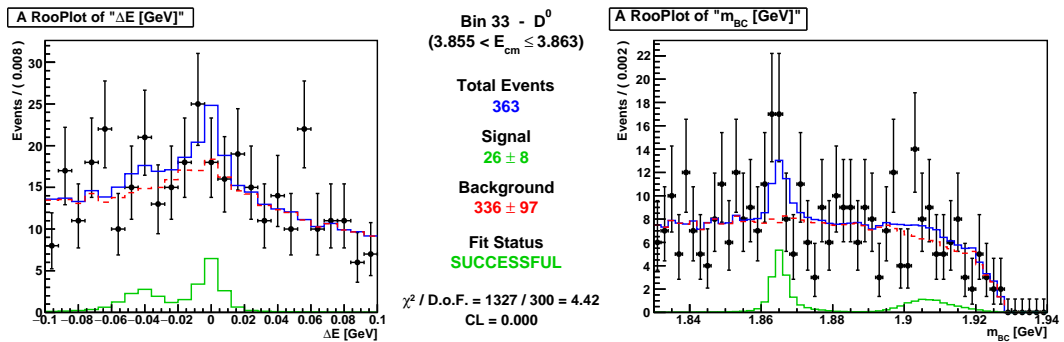
Figure B.1: Signal Fitting Plots for D^0 Bins 0 - 1.

Bin 2 - D^0
(3.737 < E_{cm} ≤ 3.744)

Total Events
174

Signal
15 ± 5

Background
158 ± 53

Fit Status
SUCCESSFUL

χ^2 / D.o.F. = 551 / 134 = 4.11
CL = 0.000

Signal Fit - D^0 Bin 2

Bin 3 - D^0
(3.744 < E_{cm} ≤ 3.746)

Total Events
650

Signal
166 ± 15

Background
483 ± 152

Fit Status
SUCCESSFUL

χ^2 / D.o.F. = 502 / 323 = 1.56
CL = 0.000

Signal Fit - D^0 Bin 3

Bin 4 - D^0
(3.746 < E_{cm} ≤ 3.748)

Total Events
1070

Signal
266 ± 20

Background
803 ± 236

Fit Status
SUCCESSFUL

χ^2 / D.o.F. = 647 / 407 = 1.59
CL = 0.000

Signal Fit - D^0 Bin 4

Bin 5 - D^0
(3.748 < E_{cm} ≤ 3.750)

Total Events
1935

Signal
508 ± 27

Background
1426 ± 373

Fit Status
SUCCESSFUL

χ^2 / D.o.F. = 557 / 489 = 1.14
CL = 0.018

Signal Fit - D^0 Bin 5

Figure B.2: Signal Fitting Plots for D^0 Bins 2 - 5.
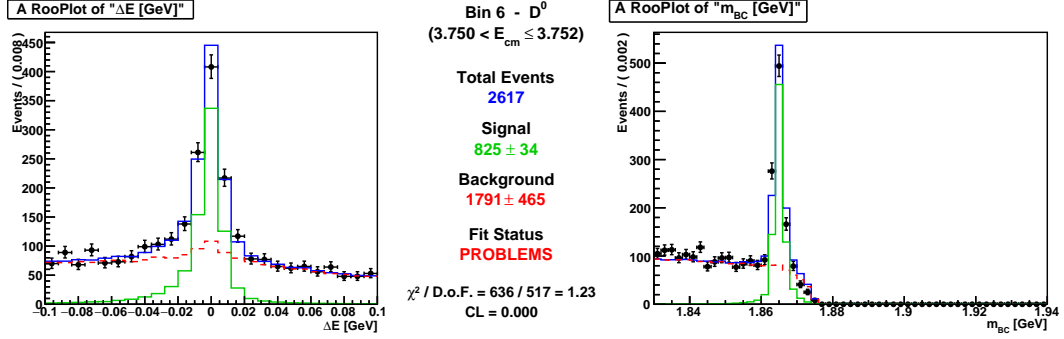
Signal Fit - D^0 Bin 6
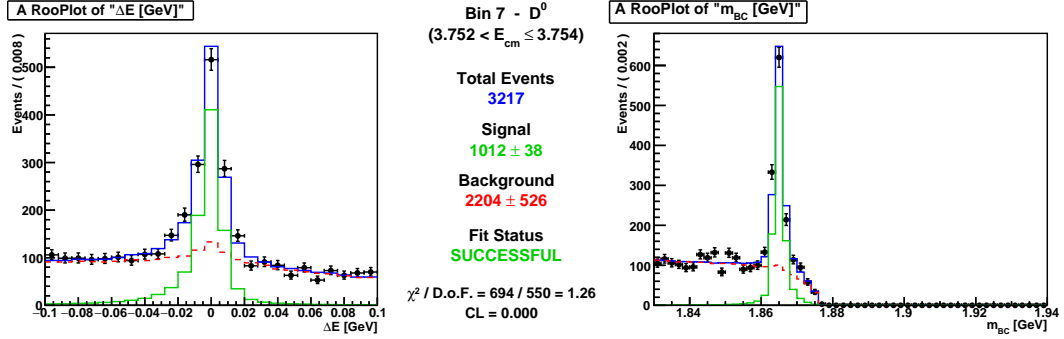
Signal Fit - D^0 Bin 7
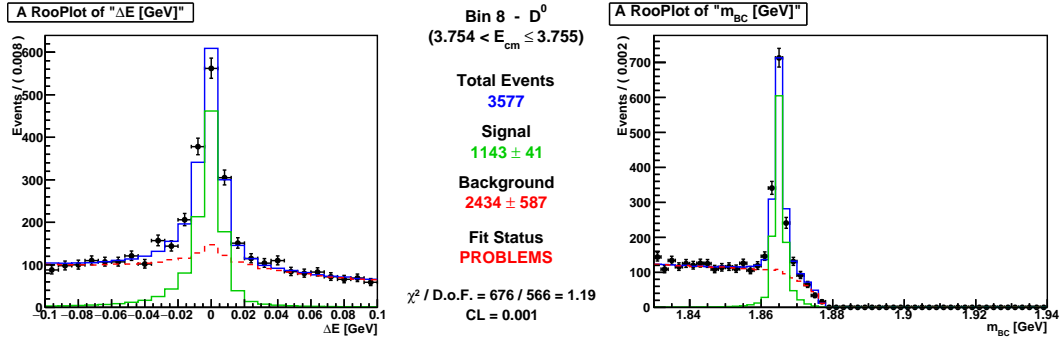
Signal Fit - D^0 Bin 8
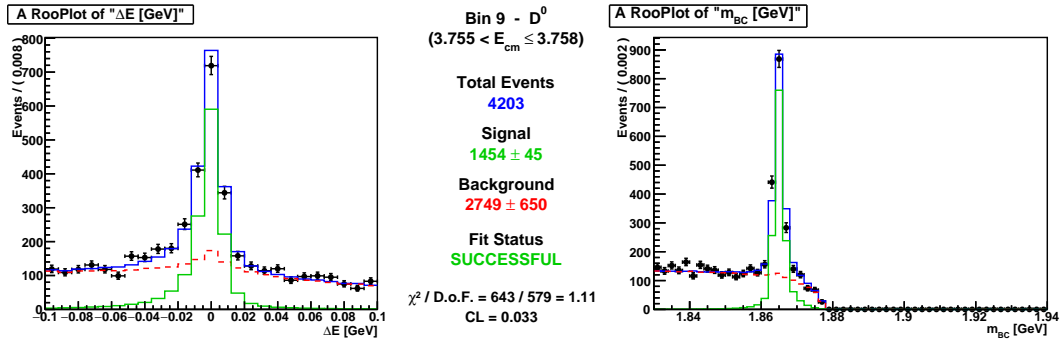
Signal Fit - D^0 Bin 9

Figure B.3: Signal Fitting Plots for D^0 Bins 6 - 9.
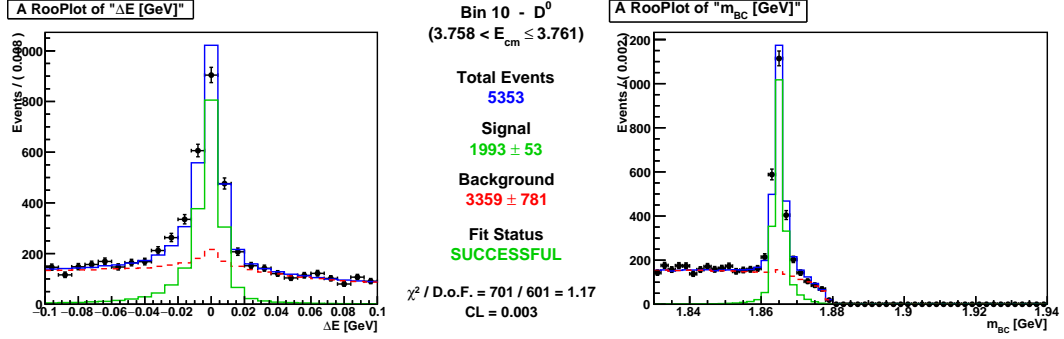
Signal Fit - D^0 Bin 10
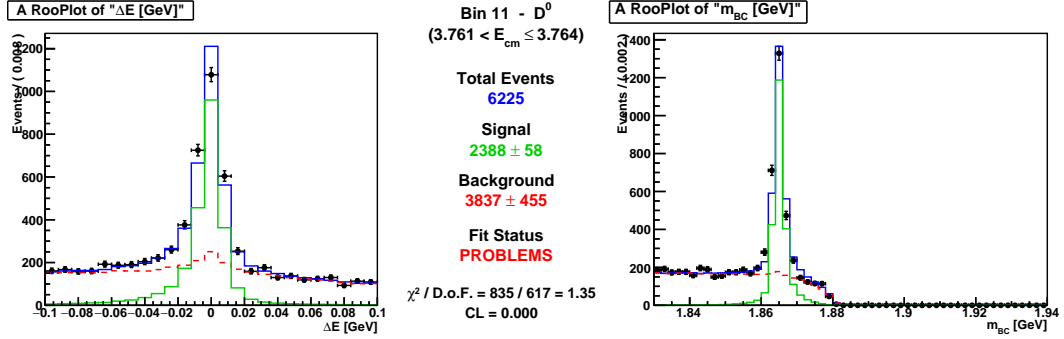
Signal Fit - D^0 Bin 11
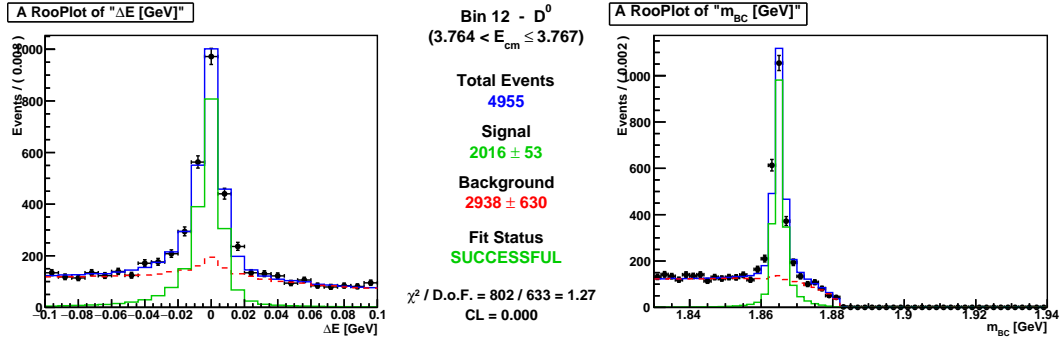
Signal Fit - D^0 Bin 12
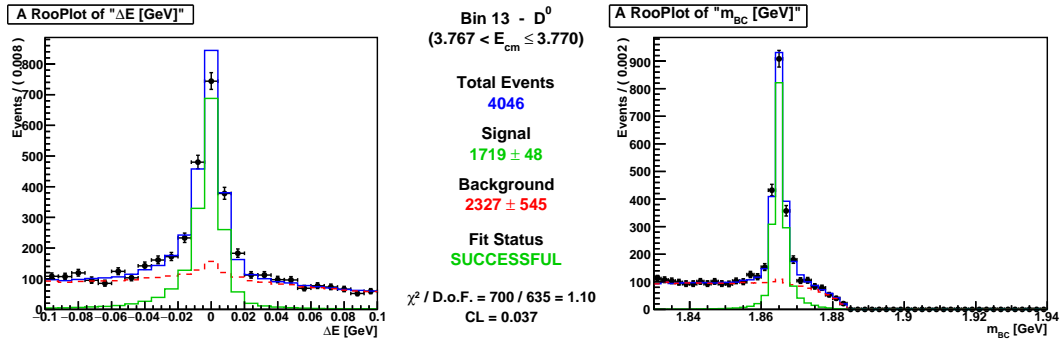
Signal Fit - D^0 Bin 13
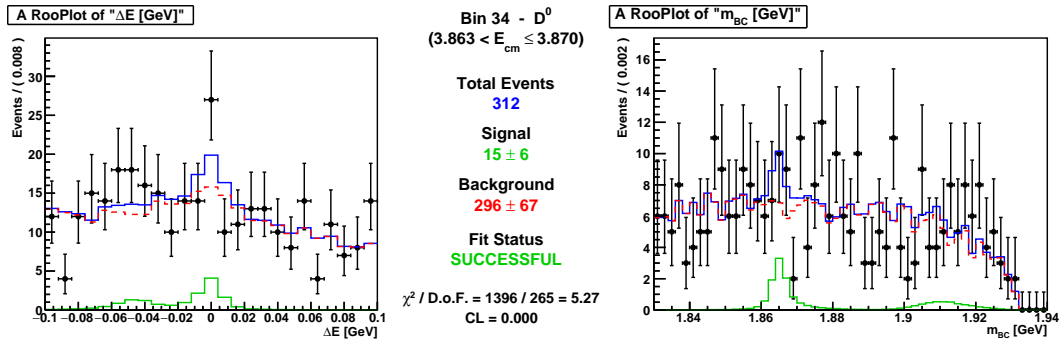
Figure B.4: Signal Fitting Plots for D^0 Bins 10 - 13.

Bin 14 - D^0
$(3.770 < E_{cm} \leq 3.773)$

Total Events
3657

Signal
1578 ± 46

Background
2079 ± 494

Fit Status
SUCCESSFUL

χ^2 / D.o.F. = 734 / 628 = 1.17
CL = 0.002

Signal Fit - D^0 Bin 14

Bin 15 - D^0
$(3.773 < E_{cm} \leq 3.776)$

Total Events
3585

Signal
1561 ± 46

Background
2024 ± 328

Fit Status
SUCCESSFUL

χ^2 / D.o.F. = 753 / 643 = 1.17
CL = 0.002

Signal Fit - D^0 Bin 15

Bin 16 - D^0
$(3.776 < E_{cm} \leq 3.779)$

Total Events
3619

Signal
1543 ± 45

Background
2076 ± 462

Fit Status
SUCCESSFUL

χ^2 / D.o.F. = 793 / 659 = 1.20
CL = 0.000

Signal Fit - D^0 Bin 16

Bin 17 - D^0
$(3.779 < E_{cm} \leq 3.782)$

Total Events
3739

Signal
1522 ± 46

Background
2217 ± 486

Fit Status
SUCCESSFUL

χ^2 / D.o.F. = 820 / 688 = 1.19
CL = 0.000

Signal Fit - D^0 Bin 17

Figure B.5: Signal Fitting Plots for D^0 Bins 14 - 17.
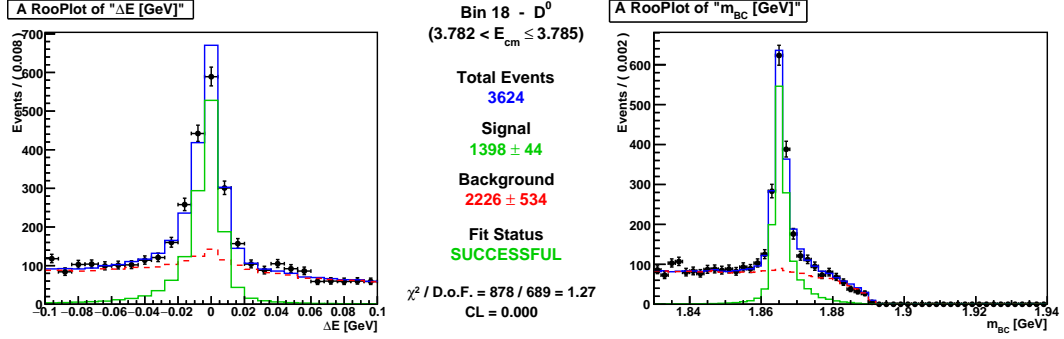
Signal Fit - D^0 Bin 18
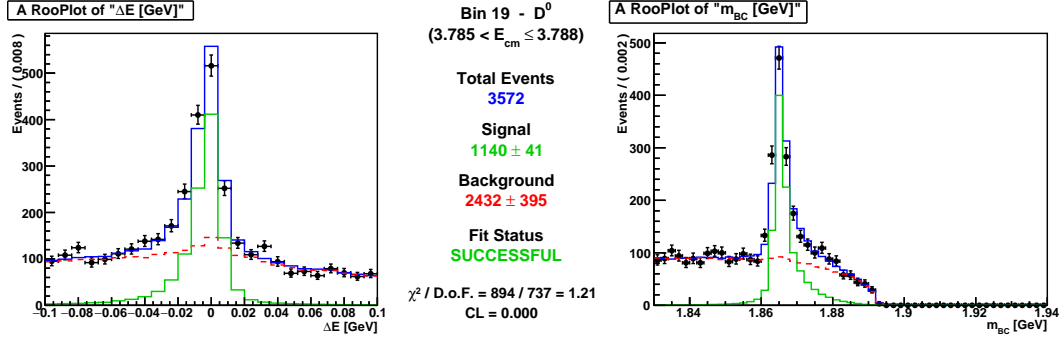
Signal Fit - D^0 Bin 19
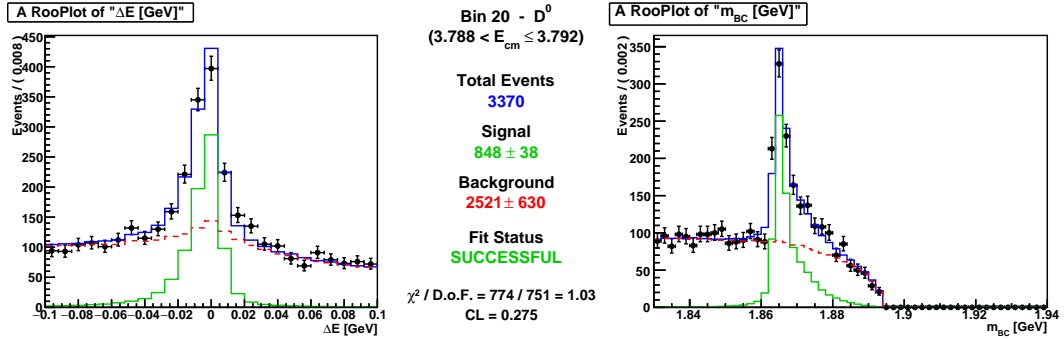
Signal Fit - D^0 Bin 20
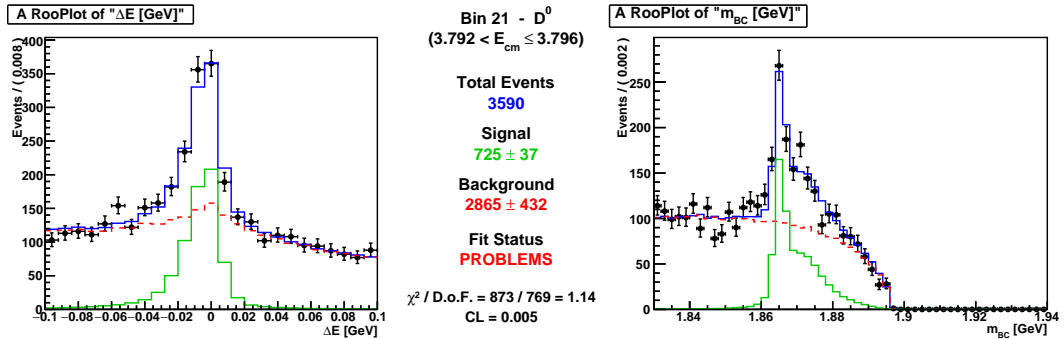
Signal Fit - D^0 Bin 21

Figure B.6: Signal Fitting Plots for D^0 Bins 18 - 21.

Bin 22 - D^0
(3.796 < E_{cm} ≤ 3.800)

Total Events
3661
Signal
514 ± 35
Background
3146 ± 729
Fit Status
SUCCESSFUL

χ^2 / D.o.F. = 919 / 808 = 1.14
CL = 0.004

Signal Fit - D^0 Bin 22

Bin 23 - D^0
(3.800 < E_{cm} ≤ 3.803)

Total Events
3349
Signal
354 ± 31
Background
2995 ± 683
Fit Status
SUCCESSFUL

χ^2 / D.o.F. = 980 / 826 = 1.19
CL = 0.000

Signal Fit - D^0 Bin 23

Bin 24 - D^0
(3.803 < E_{cm} ≤ 3.806)

Total Events
2260
Signal
194 ± 23
Background
2065 ± 1100
Fit Status
SUCCESSFUL

χ^2 / D.o.F. = 837 / 807 = 1.04
CL = 0.224

Signal Fit - D^0 Bin 24

Bin 25 - D^0
(3.806 < E_{cm} ≤ 3.809)

Total Events
1470
Signal
125 ± 19
Background
1345 ± 326
Fit Status
SUCCESSFUL

χ^2 / D.o.F. = 974 / 697 = 1.40
CL = 0.000

Signal Fit - D^0 Bin 25

Figure B.7: Signal Fitting Plots for D^0 Bins 22 - 25.
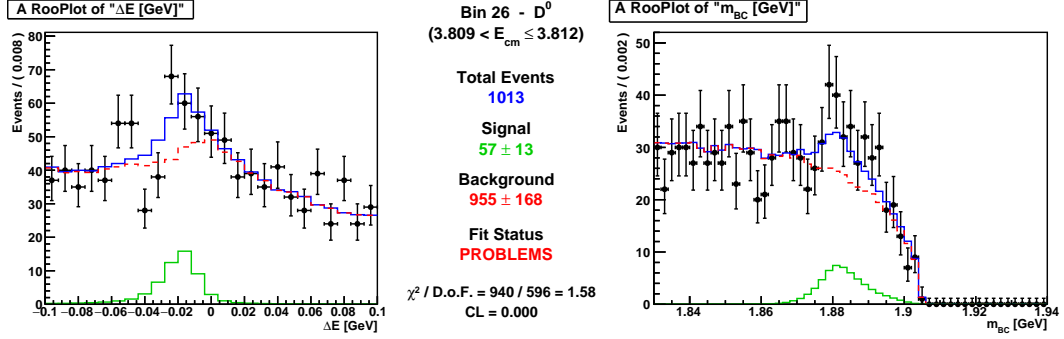
Signal Fit - D^0 Bin 26
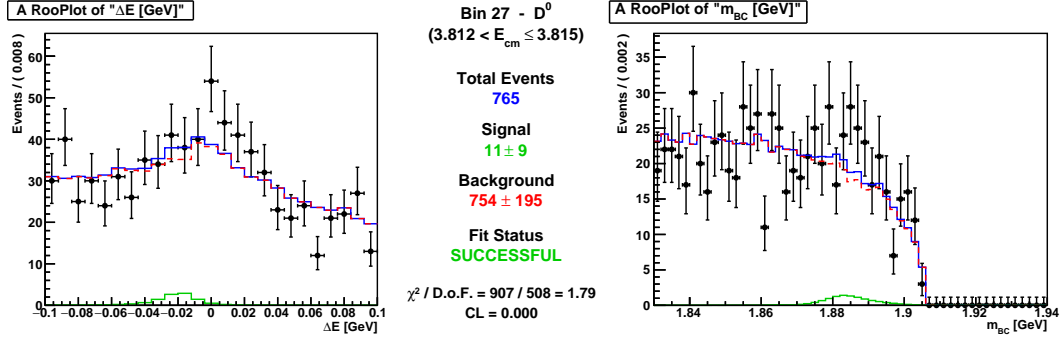
Signal Fit - D^0 Bin 27
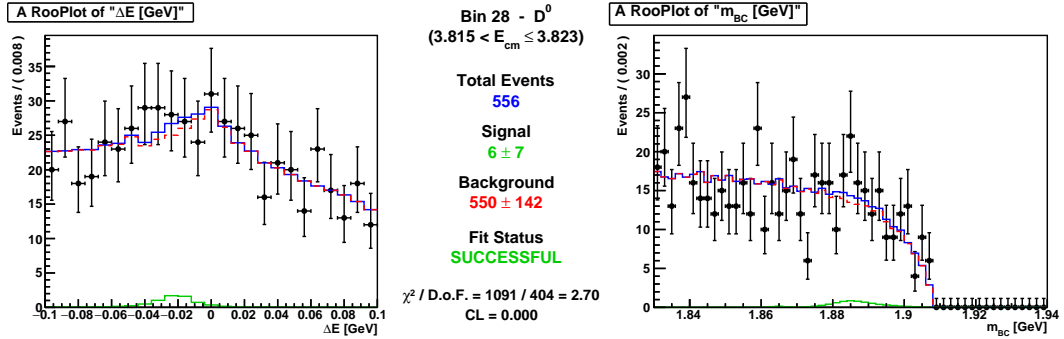
Signal Fit - D^0 Bin 28
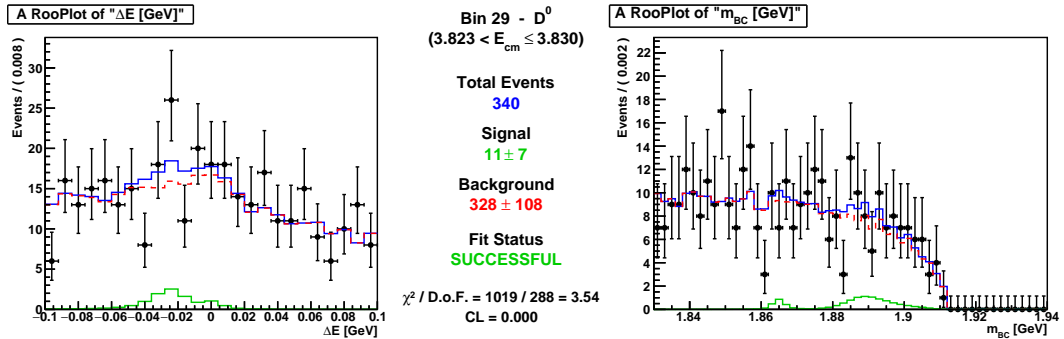
Signal Fit - D^0 Bin 29

Figure B.8: Signal Fitting Plots for D^0 Bins 26 - 29.
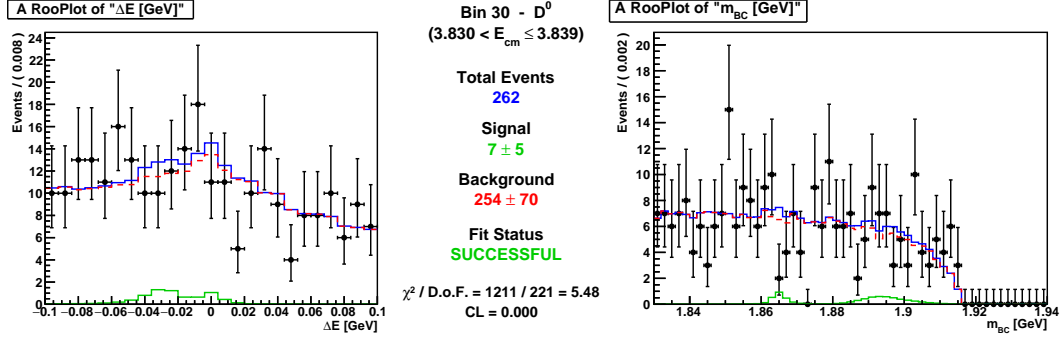
Signal Fit - D^0 Bin 30
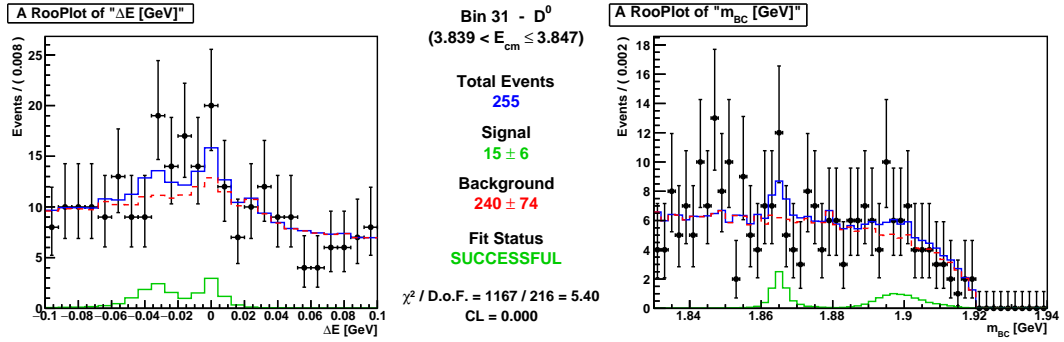
Signal Fit - D^0 Bin 31
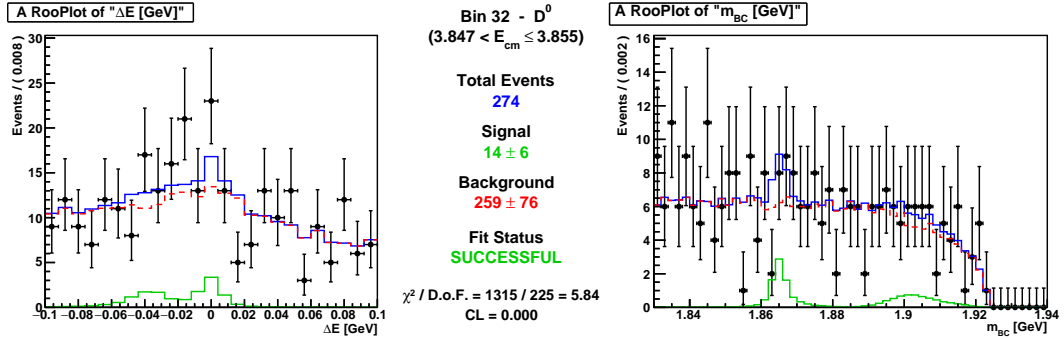
Signal Fit - D^0 Bin 32

Signal Fit - D^0 Bin 33

Figure B.9: Signal Fitting Plots for D^0 Bins 30 - 33.

Signal Fit - D^0 Bin 34

Figure B.10: Signal Fitting Plots for D^0 Bin 34.

Appendix C

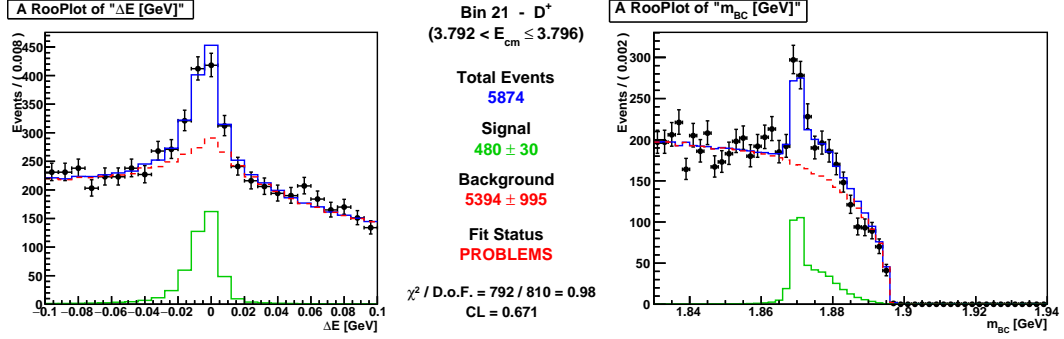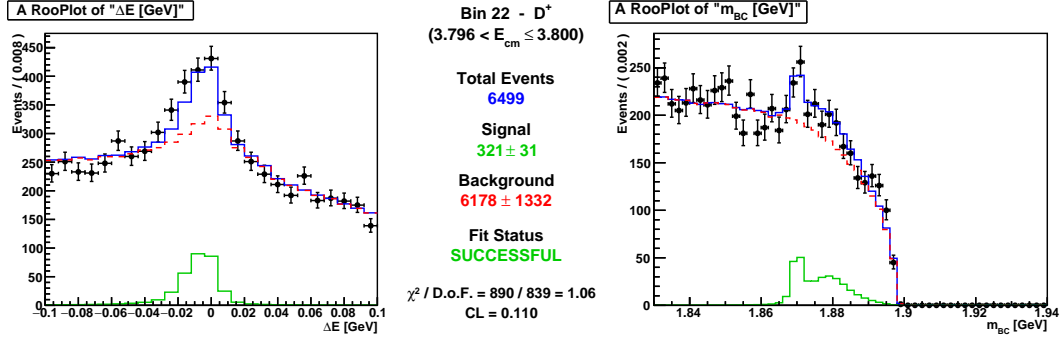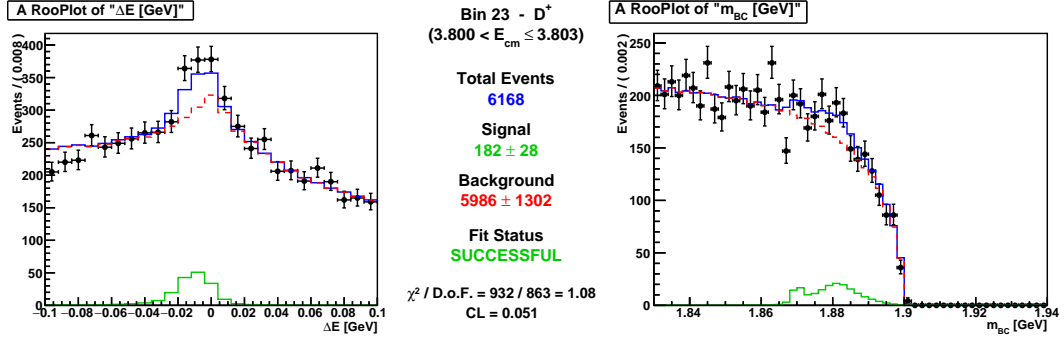# D^+ Signal Fits

Signal Fit - D^+ Bin 3
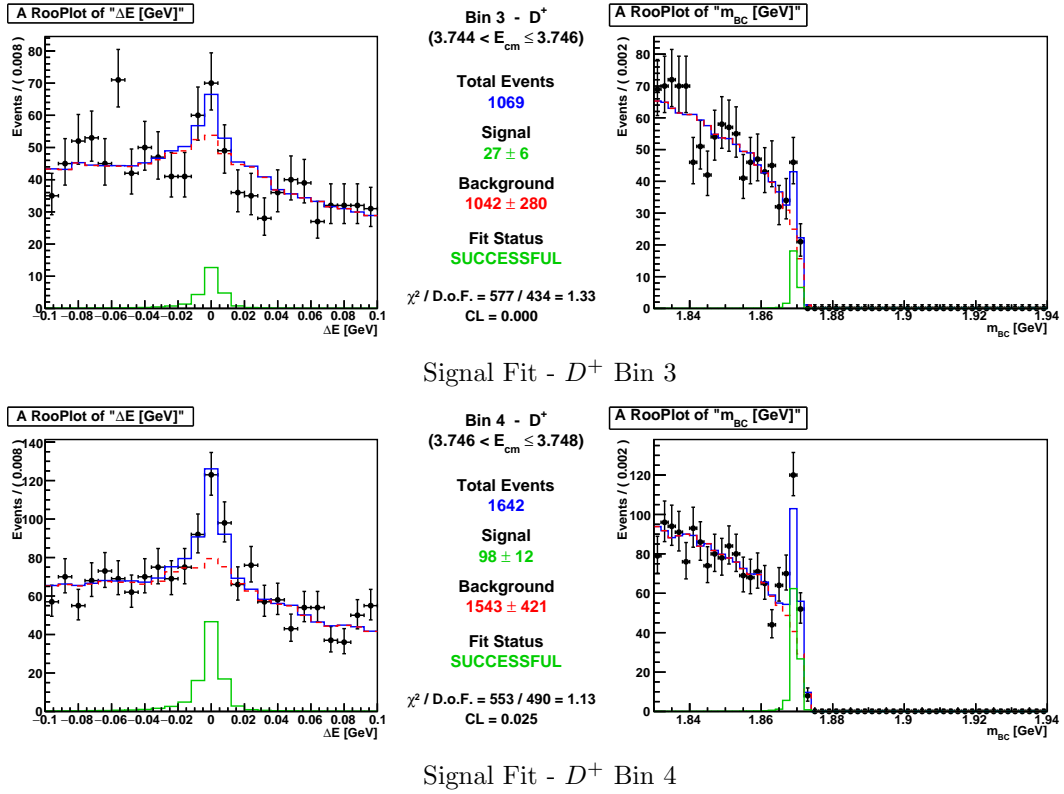
Signal Fit - D^+ Bin 4

Figure C.1: Signal Fitting Plots for D^+ Bins 3 - 4.
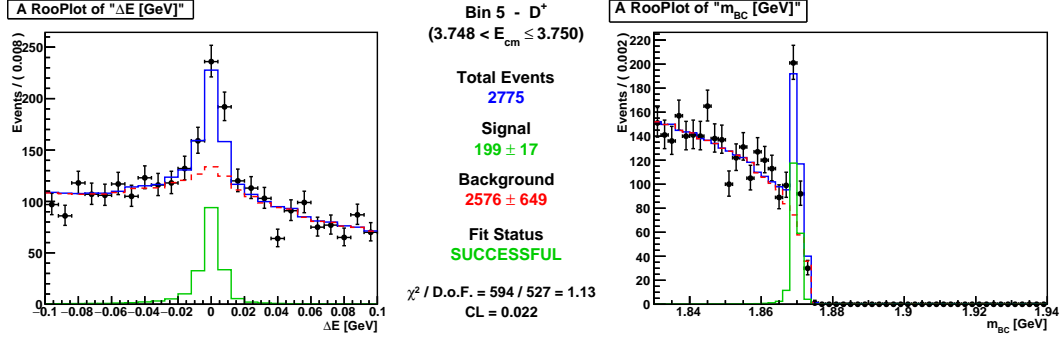
Signal Fit - D^+ Bin 5
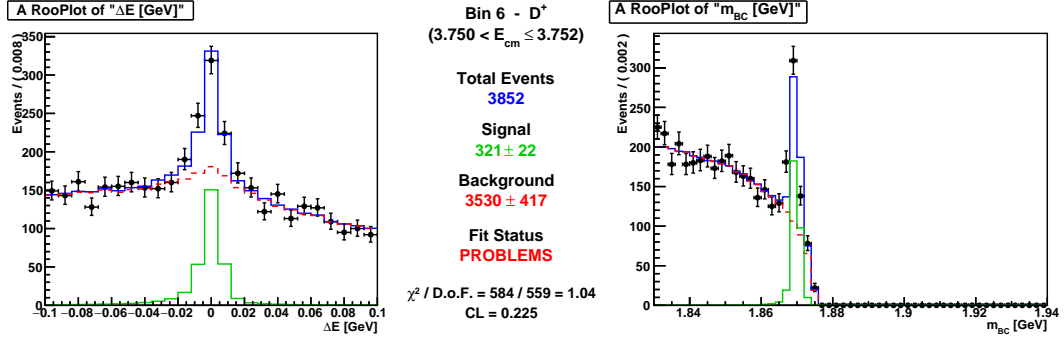
Signal Fit - D^+ Bin 6
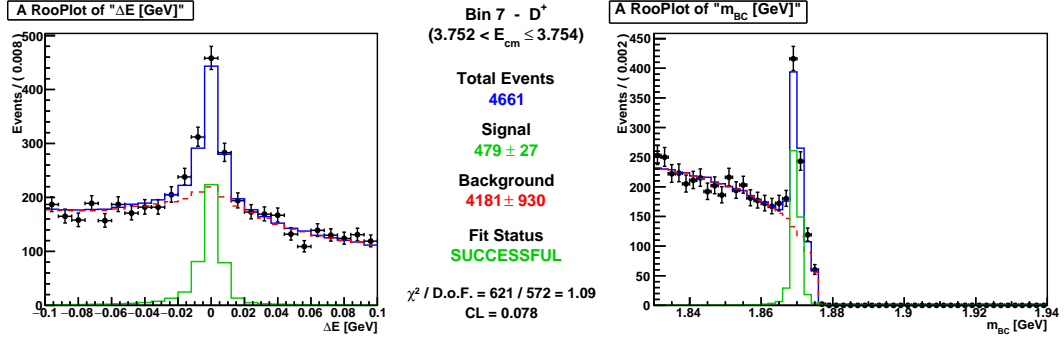
Signal Fit - D^+ Bin 7
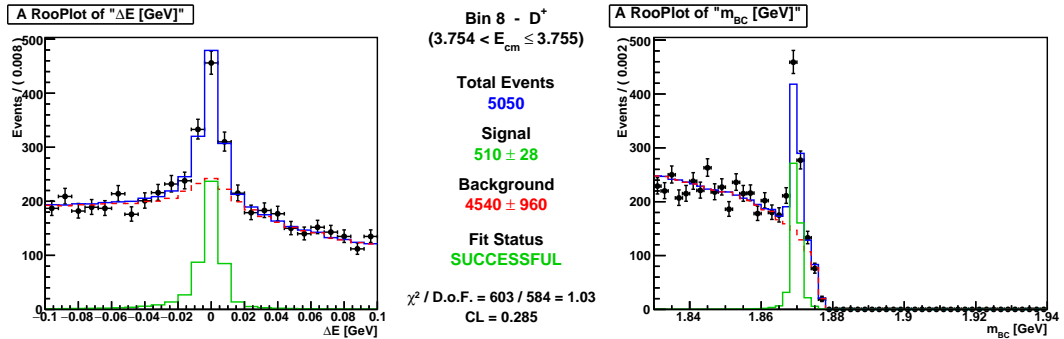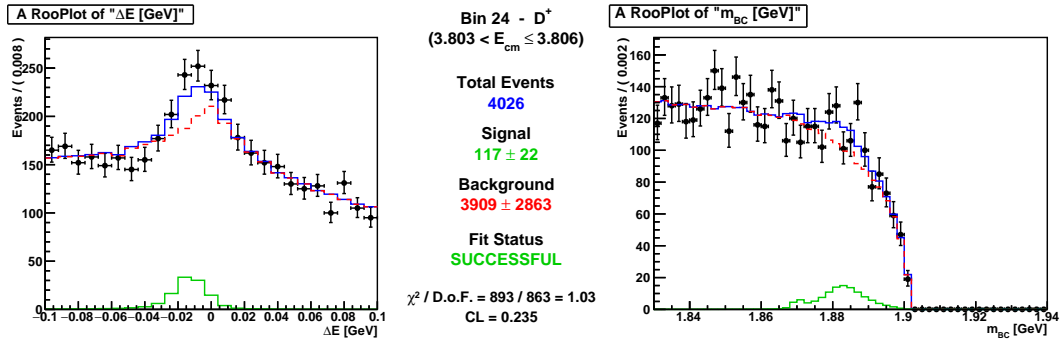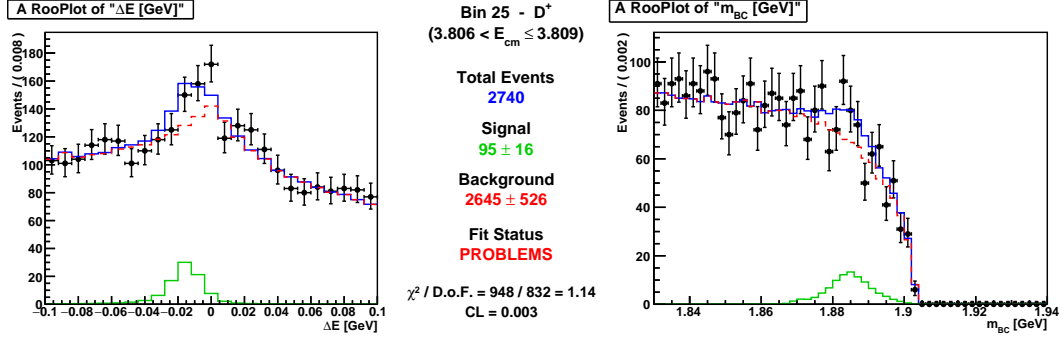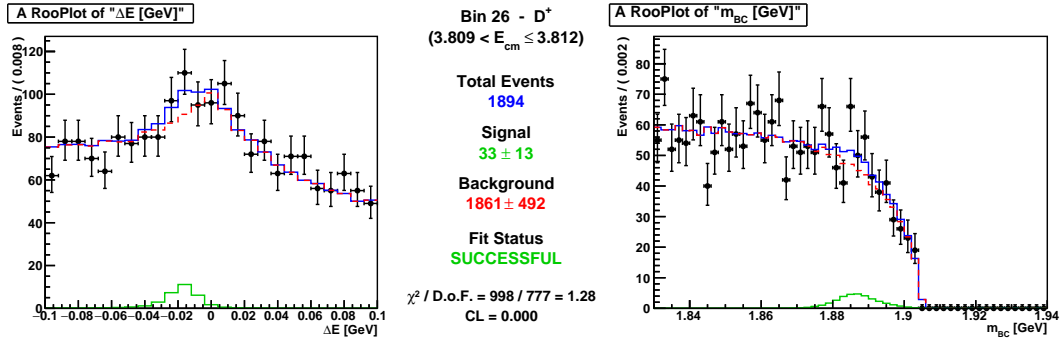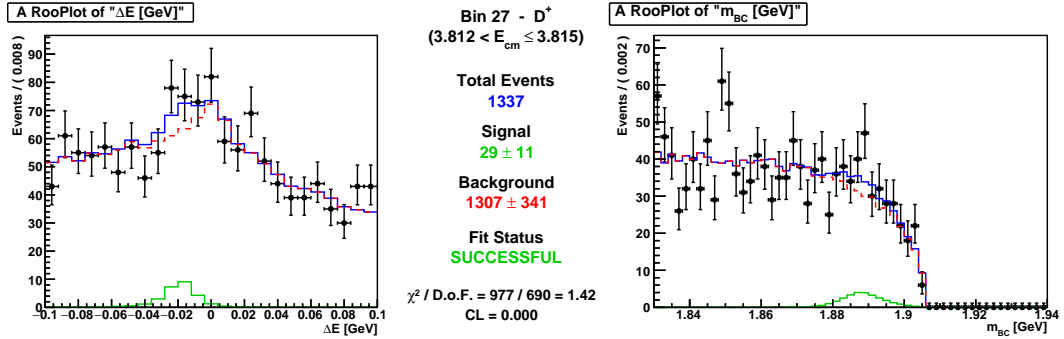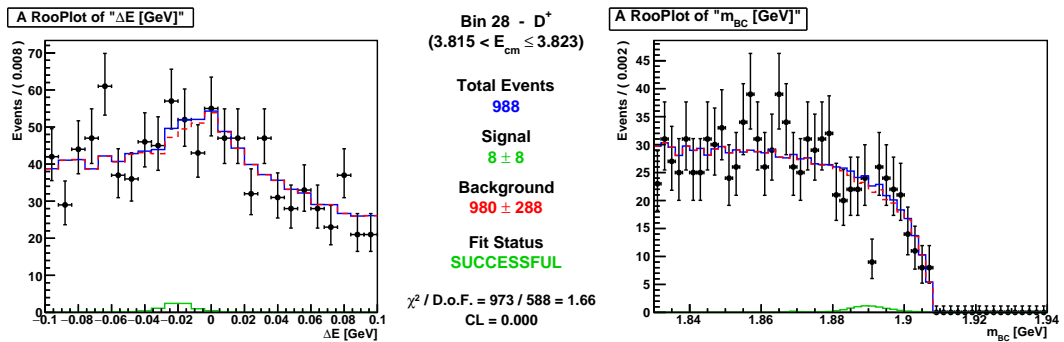

Signal Fit - D^+ Bin 8

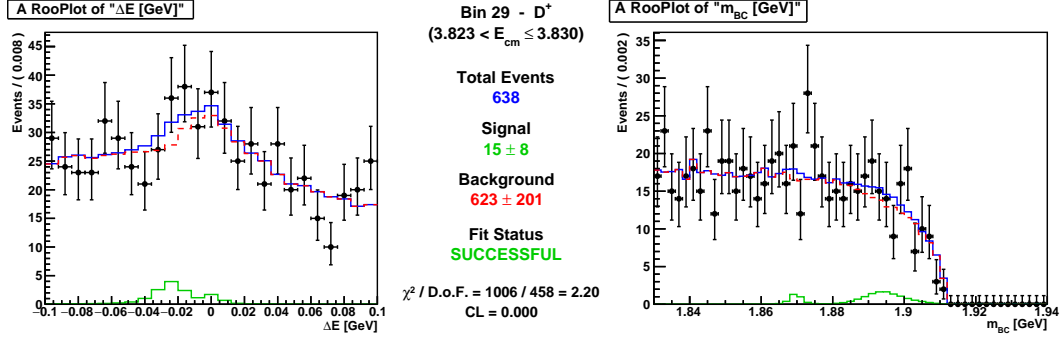Figure C.2: Signal Fitting Plots for D^+ Bins 5 - 8.

Bin 9 - D⁺
(3.755 < E_{cm} ≤ 3.758)

Total Events
5864

Signal
680 ± 32

Background
5183 ± 1075

Fit Status
SUCCESSFUL

χ² / D.o.F. = 644 / 595 = 1.08
CL = 0.081

Signal Fit - D^+ Bin 9

Bin 10 - D⁺
(3.758 < E_{cm} ≤ 3.761)

Total Events
7373

Signal
1036 ± 39

Background
6337 ± 1263

Fit Status
SUCCESSFUL

χ² / D.o.F. = 642 / 617 = 1.04
CL = 0.234

Signal Fit - D^+ Bin 10

Bin 11 - D⁺
(3.761 < E_{cm} ≤ 3.764)

Total Events
8425

Signal
1323 ± 44

Background
7101 ± 1328

Fit Status
SUCCESSFUL

χ² / D.o.F. = 676 / 634 = 1.07
CL = 0.122

Signal Fit - D^+ Bin 11

Bin 12 - D⁺
(3.764 < E_{cm} ≤ 3.767)

Total Events
6907

Signal
1224 ± 42

Background
5682 ± 1146

Fit Status
SUCCESSFUL

χ² / D.o.F. = 749 / 646 = 1.16
CL = 0.003

Signal Fit - D^+ Bin 12

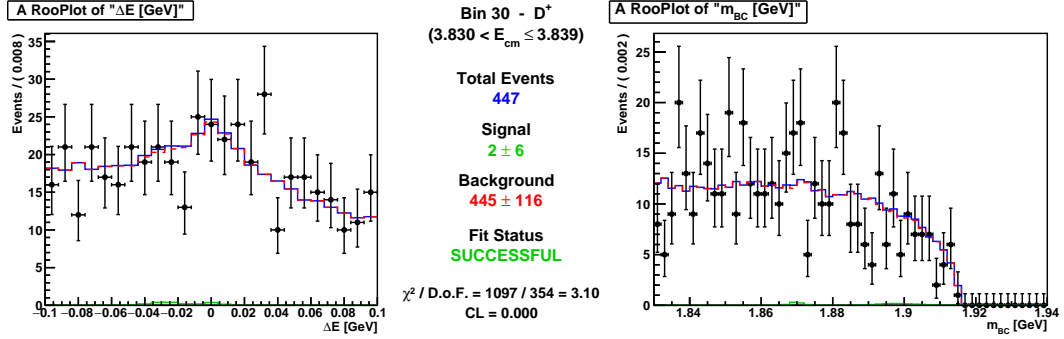Figure C.3: Signal Fitting Plots for D^+ Bins 6 - 12.
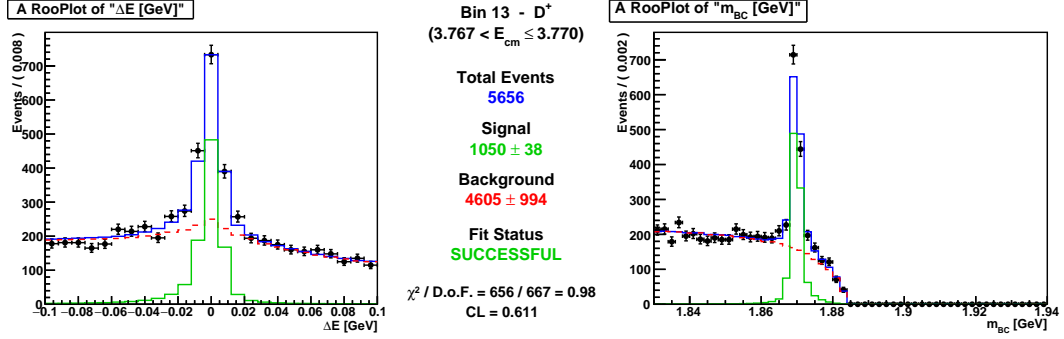
Signal Fit - D^+ Bin 13
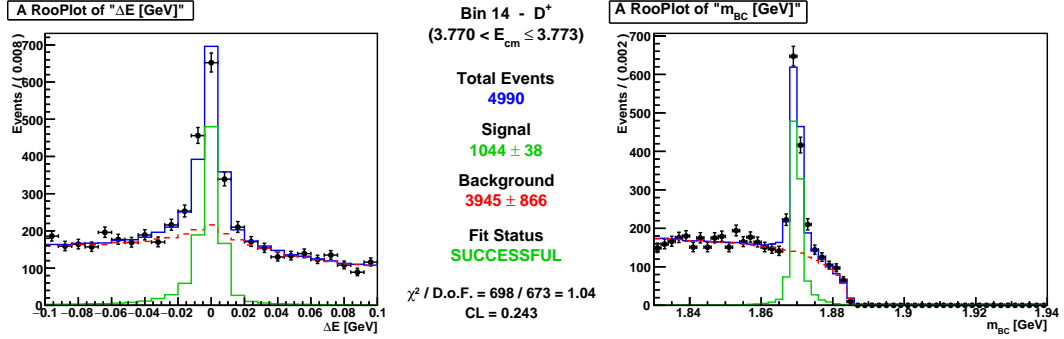
Signal Fit - D^+ Bin 14
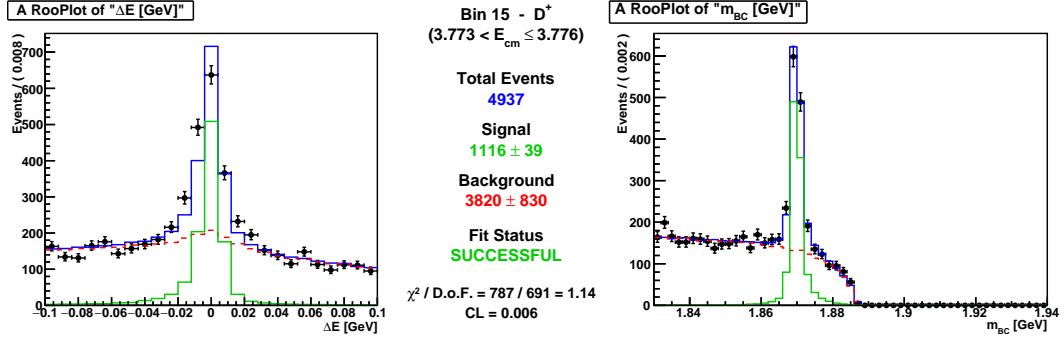
Signal Fit - D^+ Bin 15
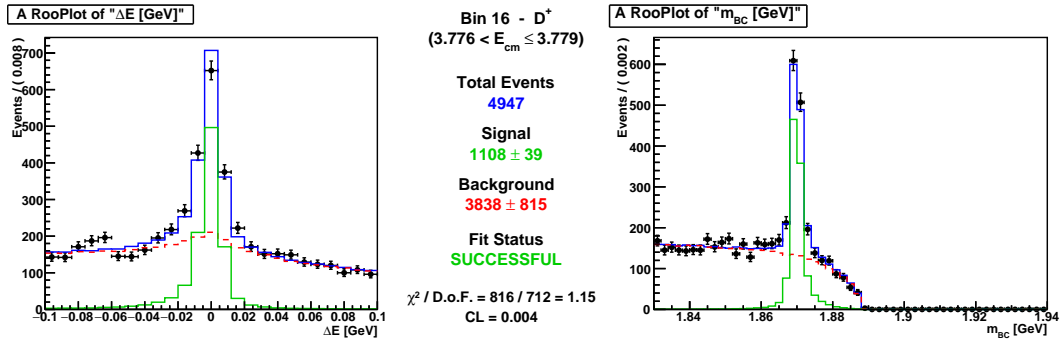
Signal Fit - D^+ Bin 16

Figure C.4: Signal Fitting Plots for D^+ Bins 13 - 16.
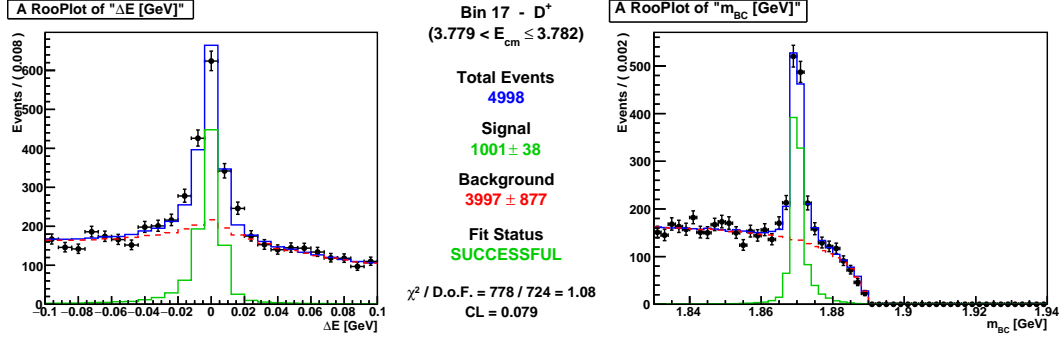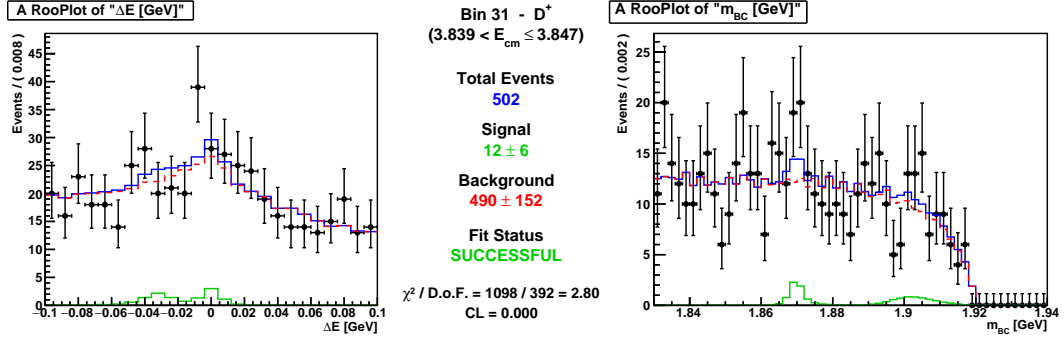
Signal Fit - D^+ Bin 17
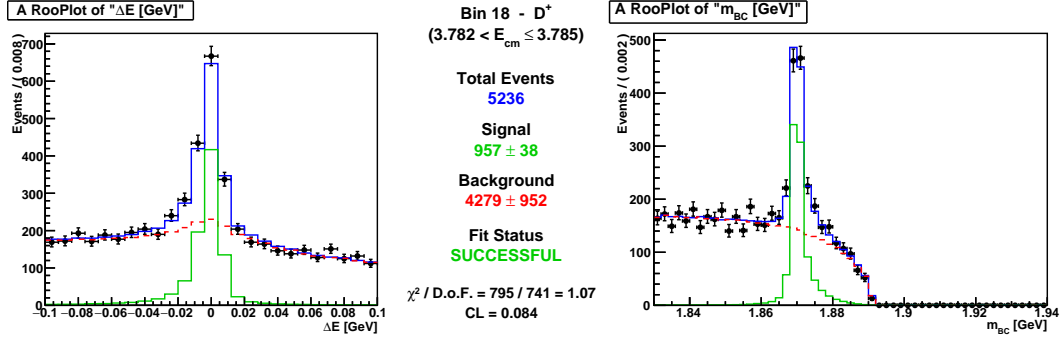
Signal Fit - D^+ Bin 18
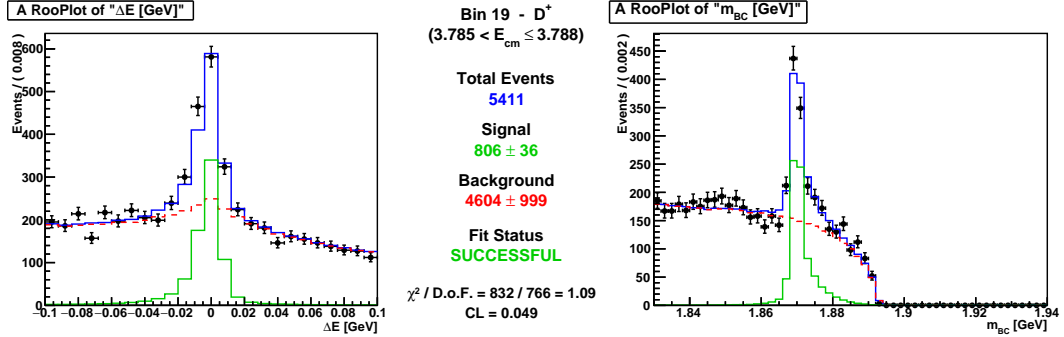
Signal Fit - D^+ Bin 19
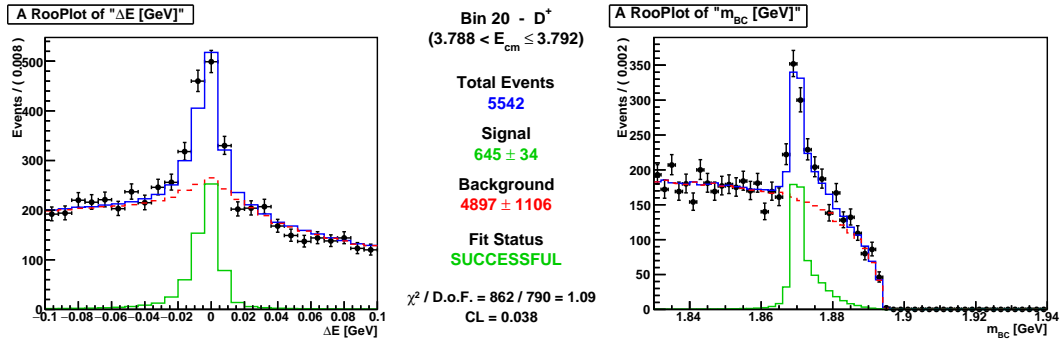
Signal Fit - D^+ Bin 20

Figure C.5: Signal Fitting Plots for D^+ Bins 17 - 20.
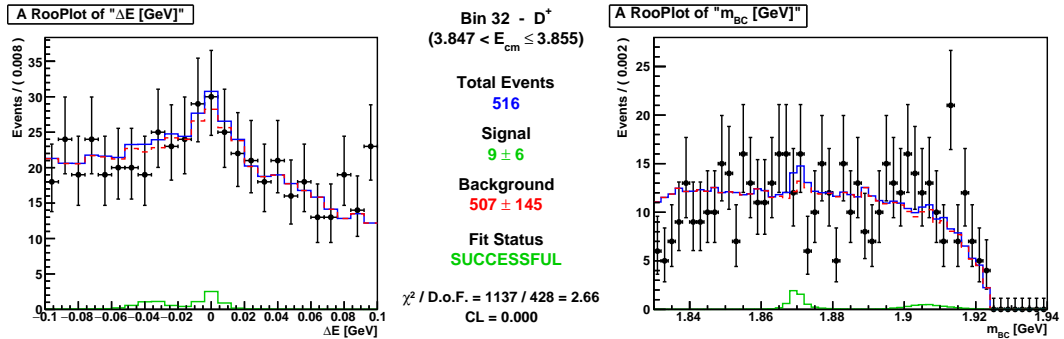
Signal Fit - D^+ Bin 21

Signal Fit - D^+ Bin 22

Signal Fit - D^+ Bin 23

Signal Fit - D^+ Bin 24

Figure C.6: Signal Fitting Plots for D^+ Bins 21 - 24.

Signal Fit - D^+ Bin 25

Signal Fit - D^+ Bin 26

Signal Fit - D^+ Bin 27

Signal Fit - D^+ Bin 28
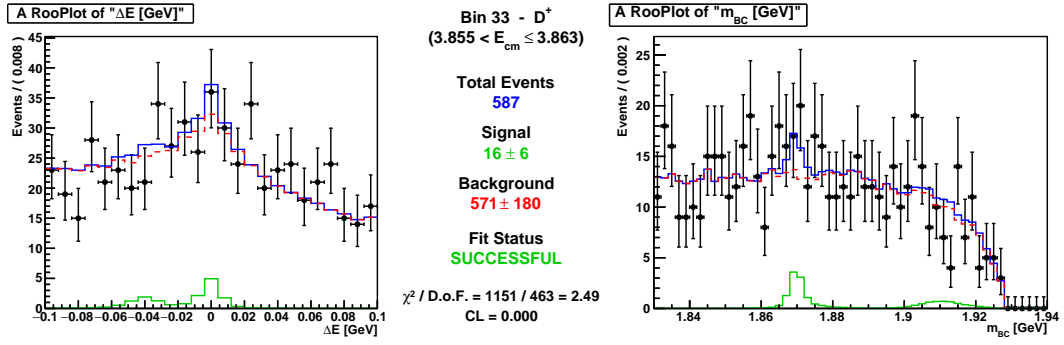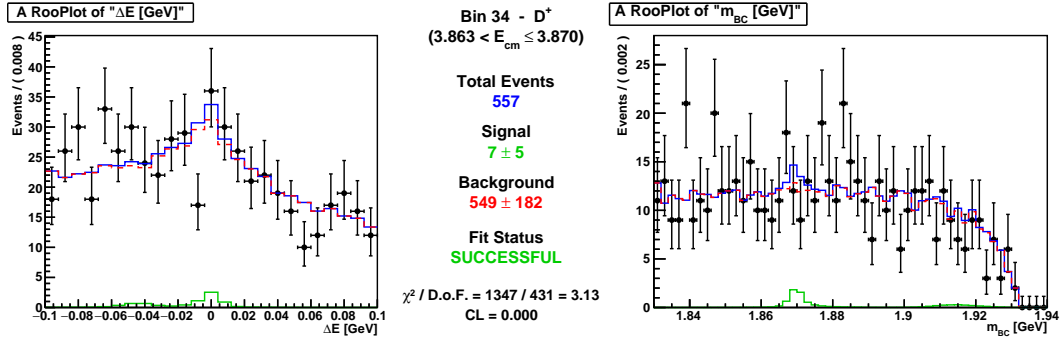
Figure C.7: Signal Fitting Plots for D^+ Bins 25 - 28.

Bin 29 - D$^+$
(3.823 < E$_{cm}$ ≤ 3.830)

Total Events
638

Signal
15 ± 8

Background
623 ± 201

Fit Status
SUCCESSFUL

χ² / D.o.F. = 1006 / 458 = 2.20
CL = 0.000

Signal Fit - D^+ Bin 29

Bin 30 - D$^+$
(3.830 < E$_{cm}$ ≤ 3.839)

Total Events
447

Signal
2 ± 6

Background
445 ± 116

Fit Status
SUCCESSFUL

χ² / D.o.F. = 1097 / 354 = 3.10
CL = 0.000

Signal Fit - D^+ Bin 30

Bin 31 - D$^+$
(3.839 < E$_{cm}$ ≤ 3.847)

Total Events
502

Signal
12 ± 6

Background
490 ± 152

Fit Status
SUCCESSFUL

χ² / D.o.F. = 1098 / 392 = 2.80
CL = 0.000

Signal Fit - D^+ Bin 31

Bin 32 - D$^+$
(3.847 < E$_{cm}$ ≤ 3.855)

Total Events
516

Signal
9 ± 6

Background
507 ± 145

Fit Status
SUCCESSFUL

χ² / D.o.F. = 1137 / 428 = 2.66
CL = 0.000

Signal Fit - D^+ Bin 32

Figure C.8: Signal Fitting Plots for D^+ Bins 29 - 32.

Signal Fit - D^+ Bin 33

Signal Fit - D^+ Bin 34

Figure C.9: Signal Fitting Plots for D^+ Bins 33 - 34.